



Published in final edited form as:

Curr Biol. 2022 August 08; 32(15): 3317–3333.e7. doi:10.1016/j.cub.2022.06.019.

Neural Network Organization for Courtship Song Feature Detection in *Drosophila*

Christa A. Baker¹, Claire McKellar^{1,3}, Rich Pang¹, Aljoscha Nern³, Sven Dorkenwald^{1,2}, Diego A. Pacheco¹, Nils Eckstein^{3,4}, Jan Funke³, Barry J. Dickson³, Mala Murthy¹

¹Princeton Neuroscience Institute, Princeton University, Princeton, NJ, USA

²Computer Science Department, Princeton University, Princeton, NJ, USA

³Janelia Research Campus, HHMI, Ashburn, VA, USA

⁴Institute of Neuroinformatics UZH/ETHZ, Zurich, Switzerland

SUMMARY

Animals communicate using sounds in a wide range of contexts, and auditory systems must encode behaviorally relevant acoustic features to drive appropriate reactions. How feature detection emerges along auditory pathways has been difficult to solve due to challenges in mapping the underlying circuits and characterizing responses to behaviorally relevant features. Here, we study auditory activity in the *Drosophila melanogaster* brain and investigate feature selectivity for the two main modes of fly courtship song, sinusoids and pulse trains. We identify 24 new cell types of the intermediate layers of the auditory pathway, and using a new connectomic resource, FlyWire, we map all synaptic connections between these cell types, in addition to connections to known early and higher-order auditory neurons - this represents the first circuit-level map of the auditory pathway. We additionally determine the sign (excitatory or inhibitory) of most synapses in this auditory connectome. We find that auditory neurons display a continuum of preferences for courtship song modes, and that neurons with different song mode preferences and response timescales are highly interconnected in a network that lacks hierarchical structure. Nonetheless, we find that the response properties of individual cell types within the connectome is predictable from its inputs. Our study thus provides new insights into the organization of auditory coding within the *Drosophila* brain.

eTOC Blurp

Author for correspondence and lead contact: Mala Murthy (mmurthy@princeton.edu).

AUTHOR CONTRIBUTIONS

Conceptualization, CAB, CM, MM; methodology, CAB, DP, SD, RP, MM; investigation, CAB, CM, AN, KT, NE, JF, BJD; formal analysis, CAB, RP, DP, SD; visualization, CAB, CM, RP; writing - original draft, CAB, RP, CM, MM; writing - review and editing, CAB, MM with feedback from all authors.

Twitter: @MurthyLab

DECLARATION OF INTERESTS

The authors declare no competing interests.

Publisher's Disclaimer: This is a PDF file of an unedited manuscript that has been accepted for publication. As a service to our customers we are providing this early version of the manuscript. The manuscript will undergo copyediting, typesetting, and review of the resulting proof before it is published in its final form. Please note that during the production process errors may be discovered which could affect the content, and all legal disclaimers that apply to the journal pertain.

Baker et al. discover and functionally characterize over 20 new auditory cell types in the *Drosophila* brain. They map synaptic connectivity among almost all known auditory neurons, and find that the auditory system is densely interconnected, suggesting that connections between differently tuned neurons are important for shaping auditory responses.

INTRODUCTION

Sounds are integral to the social lives of animals. Accordingly, brains have evolved to recognize behaviorally salient acoustic signals. For instance, courtship songs often contain information about sender status and species, and receivers must decode this information by analyzing patterns within songs¹⁻⁴. Several species produce songs comprising multiple acoustic types, often called syllables or modes⁵⁻⁷. While prior work has examined where selectivity for conspecific sounds emerges across a variety of systems including songbirds⁸, primates⁹, and mice¹⁰, the circuit mechanisms shaping selectivity are unknown. For example, while a hypothesized circuit for recognizing stereotyped songs has been described in crickets^{11,12}, connectivity among these neurons has not yet been determined, and cricket songs comprise only a single mode. Understanding how auditory systems establish selectivity for conspecific sounds requires linking responses to different song types with neuronal connectivity, a significant challenge in larger brains. Here we focus on *Drosophila melanogaster*, a species with a compact brain and both genetic and connectomic tools for circuit dissection.

D. melanogaster males alternate between two major song modes during courtship: pulse and sine song (Figure 1A; ^{13,14}). The composition of song bouts (the duration of each mode and switches between them) are dependent on sensory feedback from the female¹⁵. Receptive females reduce locomotor speed in response to multiple features within conspecific song, from the frequency of individual elements to longer timescale patterns such as the average duration of song bouts^{16,17}. However, how tuning for these features emerges along the auditory pathway is not known.

Sound detection begins at the *Drosophila* antenna, within which Johnston's organ neurons (JONs) detect sound-evoked vibrations of the arista¹⁸. Since fly hearing organs are sensitive to the particle velocity component of sounds, which decreases rapidly with distance¹⁹, flies can only hear nearby sounds - primarily communication signals from conspecifics. JONs are coarsely frequency-tuned and project roughly tonotopically to the antennal mechanosensory motor center (AMMC) in the brain²⁰. This tonotopy appears to be strengthened in downstream areas, like the wedge (WED)²⁰ and ventrolateral protocerebrum (VLP)²¹ (Figure 1B). The auditory responses of a few AMMC neurons have been characterized²²⁻²⁵, and one of these, B1, is thought to be part of a major pathway for song processing^{26,27}. Downstream of the AMMC, only a handful of auditory neurons have been identified^{16,17,25,28,29}, and for most of these cell types, song coding has not systematically been examined.

Although pan-neuronal imaging found both pulse and sine responses throughout the brain²¹, we do not yet know how auditory circuits are organized, and whether song feature tuning is sharpened along the pathway hierarchically. In one model of network organization, pulse-

and sine-preferring neurons constitute separate pathways, and hierarchical organization within each pathway sharpens tuning to generate strong song mode preference. Support for this model comes from work on higher-order pulse song preferring neurons^{16,29,30} that connect with descending neurons (neurons with dendrites in the brain and axons in the ventral nerve cord) driving sex-specific behaviors; however no sine-tuned neurons have yet been identified. In a second extreme, pulse and sine preference might arise early in the pathway, and interconnections between neurons with different song mode preferences might act to diversify responses to song features.

We address these outstanding issues here, by uncovering the network organization underlying song processing in the *Drosophila* brain. We recorded auditory responses from a new collection of split-GAL4 lines, and found 24 novel auditory cell types, as well as new lines for known auditory neurons. We systematically characterized each cell's preference for sine vs. pulse song, in addition to tuning for sine frequency and pulse rate, discovering a continuum of song mode preferences among auditory neurons. Using FlyWire, a whole brain connectomic resource³¹, we mapped synaptic connectivity (in addition to the sign of connections, whether inhibitory or excitatory) among neurons. Rather than being organized into separate streams for sine and pulse processing, we discovered a complex network architecture with dense interconnectivity between cell types with different song responses and without hierarchical structure. Preference for sine and pulse song arises early in the pathway, and using a linear dynamical system model, we showed that neural responses could be predicted by the responses of their inputs. Finally, we found that the time courses of neural responses are matched to natural song statistics. These results reveal how sensory responses are shaped by connectivity within the auditory system of *Drosophila*.

RESULTS

Identifying cell types of *Drosophila* auditory circuits

To identify new cell types downstream of known early auditory neurons³¹, we focused on three of the five areas to which second-order mechanosensory neurons in the AMMC send projections³²: the wedge (WED), anterior ventrolateral protocerebrum (AVLP), and posterior ventrolateral protocerebrum (PVLP) (Figure 1B). Several higher-order auditory neurons have projections in these areas^{16,25,28,29}. We created sparse and specific split-GAL4 lines targeting such neurons (hereafter referred to as WED/VLP neurons), and then screened the most promising lines for auditory responses (Figure 1C); our goal was not to create a line for every cell type in the WED/VLP (of which over a thousand are estimated to exist³³), but to identify new auditory neuron types. In total, we examined the expression of 1041 split-GAL4 lines, generated stable lines for 117 with the sparsest expression in the brain, and selected 65 for functional recordings. These 65 lines target at least 50 WED/VLP cell types that include local, intra-hemispheric projection, and commissural neurons (Figure 1D, Data S1A).

To uncover cell type diversity within each split-GAL4 line, we collected multicolor flip-out (MCFO) images (see Methods). Most split-GAL4 lines contained morphologically similar neurons, with some heterogeneity within particular lines (Data S1B). As morphologically similar neurons may have different synaptic partners³³, we were unable to disambiguate

further any individual subtypes within each line on morphological criteria alone, and consider the WED/VLP neurons in each line a ‘cell class’. We named each cell class by identifying the neuropil with the highest density of neural processes (Table S2). We refer to the neurons imaged in each line by these names, except for auditory neurons previously named (i.e., A2, B1, B2, and WED-VLP) (Table S2)^{23,25}. To clarify which cells we targeted in each line for calcium imaging, we digitally segmented WED/VLP neurons from the broader expression pattern of each line (Figure 1E–G and Data S1C).

We tested each cell type for auditory responses using GCaMP6s³⁴ and three stimuli: pulse, sine and broadband noise (Figure 1C; see Methods). Pulse and sine constitute the two major modes of *D. melanogaster* courtship song, and noise was included to identify responses to acoustic features outside the range of parameters in song. We used intensities within those produced during natural courtship³⁵ (5 mm/sec for pulse and sine, and 2 mm/sec for noise). We found consistent auditory responses in 28 lines (43%) (Figure 1H), including four cell classes representing known auditory neurons: A2, B1, B2, and WED-VLP (Figure 2; Table S2). An additional 11 cell classes (17%) were classified as infrequent responders because responses occurred in fewer than 15% of imaged flies (Figure 1H). The remaining 26 cell classes did not respond to acoustic stimuli. Some auditory neurons were previously classified as lateral horn neurons, but not known to be auditory (e.g., AVLP_pr05 resembles AVLP-PN1 and IPS_pr01 resembles WED-PN1³⁶), while others have morphologies similar to neurons that process other mechanosensory stimuli, such as wind (e.g., WED_pr01 is distinct from but morphologically similar to the WPN neurons that encode wind direction³⁷ and to the WPNBs, whose function has not yet been characterized³⁸). In sum, our screen identified a total of 24 new auditory cell types. Using FlyWire³⁹, we identified these cell types in both hemispheres within an electron microscopic (EM) volume of an entire female brain (Figure 2; see Methods), and used the EM data below to examine connectivity between auditory cell types.

Preferences and tuning for courtship song modes among WED/VLP neurons

We determined the preference of each auditory cell type for three stimuli: sine, pulse, and noise (Figure 3A). We evaluated preference for song (pulse or sine) vs. noise (Figure 3B) and pulse vs. sine (Figure 3C and Figure S1A–B) in each fly imaged (see Methods). Our noise stimulus was filtered to contain frequencies present in song, but lacked the temporal structure of song stimuli (Figure 1C). The overwhelming majority of neurons preferred song stimuli (pulse or sine) over noise (Figure 3B), with no correlation between song vs. noise preference and song mode (pulse vs. sine) preference. Neurons that preferred the noise stimulus (WED_pr01, AVLP_pr05, and WED_VLP) nonetheless produced significant responses to song and were tuned to particular sine frequencies or pulse rates (Figure 4).

Prior work on *Drosophila* auditory neurons uncovered largely pulse-preferences^{16,28,29}, even though males spend the majority of their time singing sine song¹⁵. By sampling a larger population of cell types, we found that song mode preferences across neurons fell along a continuum (Figure 3C), with 31% pulse-preferring, 31% sine-preferring, and the remaining 38% showing intermediate preference (responding to pulse and sine stimuli roughly equally). In the subset of recordings with net inhibition (Figure S1C), pulse-

preferring neurons tended to have sine-preferring inhibition, and vice versa, suggesting that inhibition contributes to establishing auditory preferences. We next re-analyzed 19,036 regions of interest spanning the central brain of 33 flies imaged pan-neuronally²¹ according to the criteria established here, and uncovered a similar continuum (Figure 3D). This suggests that the song mode preferences of the 28 WED/VLP cell types recorded here may underlie responses brain-wide. In support of this, WED/VLP auditory neurons send projections throughout the central brain, independent of song mode preference (Figs. 3 and 4), including to regions considered primarily visual (ie, posterior lateral protocerebrum) and olfactory (i.e., lateral horn) (Figure S2). Finally, some cell types exhibited more variability in song mode preference than others (Figure 3C), either across-trials or across-animals (Figure S1D–F), but we found a similar range of variability scores within each song mode preference class.

Both males and females change their locomotor speed most in response to conspecific pulse rates (peaked at 35–40 ms interpulse intervals) and sine frequencies (ranging from 150–400 Hz)¹⁶. We therefore examined tuning for pulse rate and sine frequency, using stimuli at an intensity of 4 mm/s, which is within the range produced by males³⁵ (Figure 4A). We observed a diversity in tuning patterns to these stimuli across cell types (Figure 4B). For each preference category (sine-preferring, pulse-preferring, or intermediate), we sorted tuning curves from each recorded fly by tuning type (low-pass, bandpass, high-pass, or band-stop (see Methods)). For pulse rate tuning, sine-preferring neurons were most likely to exhibit low-pass responses (Figure 4C and 4F; consistent with these neurons preferring sinusoids over pulses since the fastest pulse rates begin to approximate sinusoids), while intermediate-preference (Figure 4D) and pulse-preferring (Figure 4E) neurons showed more diversity in pulse rate tuning. Surprisingly, relatively few recordings (2 flies from AVLP_pr36 and 1 fly each from SAD_pr01, SAD/AMMC_pr01, and AVLP_pr35) exhibited band-pass tuning for the conspecific pulse interval (35–40 ms). This is in contrast with cell types tuned for conspecific intervals found in regions downstream from the WED/VLP (e.g., pC21¹⁶ and vpoEN²⁹). Our results suggest that WED/VLP responses may serve as a set of building blocks for generating band-pass tuning downstream. For sine frequency stimuli, most responses showed low-pass or band-pass tuning, with roughly equal numbers in these two categories (Figure 4C–E, lower plots and Figure 4G). Recordings from pulse-preferring neurons (Figure 4E) predominantly showed band-pass frequency tuning centered on conspecific pulse carrier frequencies (e.g. around 250 Hz⁴⁰), whereas recordings from sine-preferring (Figure 4C) or intermediate preference neurons (Figure 4D) showed either low- or band-pass frequency tuning, with individual tuning curves tiling the broad range of frequencies present in conspecific sine song (100–400 Hz)¹⁴. Finally, principal components analysis on responses to pulse rates and sine frequencies showed that, instead of distinct clusters, the population we recorded from (131 recordings from 30 cell types) constituted a continuum from pulse- to sine-preferring, with intermediate preference neurons in the middle (Figure 4H).

The connectome of *Drosophila* auditory neurons

Several models of network organization would be consistent with the continuum of preferences for sine and pulse song, as well as diversity of tunings for sine frequency and

pulse rate (Figure 5A). In one extreme (“Model 1”), pulse- and sine-preferring responses occur in largely separate pathways, with either their own or shared intermediate preference neurons. Model 1 is supported by our analysis of LM images of each cell type (Data S1C), in which we found some spatial segregation of sine- and pulse-preferring neurons in the VLP (Figure S3), suggesting a separation between pathways. In the second extreme, pulse and sine preference already occur early in the pathway, and the continuum of responses arises through extensive interconnectivity between cell types with different preferences. Inhibitory interactions between cell types with different song mode preferences could act to sharpen or diversify tuning. Of course, the real wiring diagram could fall between these two extremes.

To test these hypotheses, we mapped synaptic connectivity among all auditory neurons (both WED/VLP neurons and previously characterized auditory neurons). We identified and proofread these neurons in *both hemispheres* of a whole brain electron microscopic volume (FlyWire)³⁹ (Figure 2, 5B), determined the number of synaptic connections via automated synapse detection⁴¹ (Figure S4A), and used a deep learning-based classifier to predict the neurotransmitter used by each cell type⁴² (Figure S5A–C). This classifier used neural networks trained on manually identified synapses to predict with high accuracy the neurotransmitter type of individual synapses. We defined the neurotransmitter of each neuron as the predicted majority neurotransmitter over all its automatically detected synapses⁴³ (see Methods). We found that pulse-preferring neurons were overwhelmingly cholinergic, whereas sine-preferring and intermediate neurons included a mix of GABAergic and cholinergic neurons (Figure 5C). We also found one dopaminergic neuron in the pulse-preferring AVLP_pr04 cell type.

Using the dimensionality reduction method UMAP⁴⁴, we clustered auditory neurons based on their connectivity patterns (Figure 5D). Neurons of a cell type tended to cluster, indicating similarity of inputs and outputs, but we found limited clustering between different cell types - instead, we observed dense interconnectivity throughout the network (gray lines), more consistent with model 2. However, there were more sine-preferring and intermediate neurons in the middle of the graph (Figure 5E–F), and pulse-preferring neurons at the ends of the graph (Figure 5G), suggesting some preferential connectivity within a preference category. To examine this, we collapsed neurons by cell type (Figure 5H and Figure S5D–F), which highlighted extensive interconnectivity between cell types with different song mode preferences, again more consistent with model 2. For example, intermediate preference WED-VLP neurons receive inputs from all preference classes, and in turn send outputs to three pulse-preferring (vpoEN, vpoIN, and pC2I) and three sine-preferring (AVLP_pr01, AVLP_pr22, and AVLP_pr31) neurons. While the auditory connectome generated here is still incomplete, these data nonetheless reveal a lack of segregation of neurons into pulse and sine song processing pathways.

We also observed a mix of excitatory and inhibitory connections throughout the network (Figure 5H; Figure S5D–F). Inhibitory connections were most common between intermediate preference and pulse-preferring neurons (Figure S5G), suggesting that this connection type may be especially important for establishing responses to pulse song features. Sine-preferring neurons provided inhibition to both pulse and intermediate

preference neurons, suggesting one major role for sine-preferring inhibitory neurons is to oppose responses to sine song (Figure S5G). The most frequent connection type was pulse-preferring neurons exciting other pulse-preferring neurons (Figure S5H) - many of these connections were in the sub-network of pulse-preferring neurons that includes descending neurons pMN1/DNp13 and pMN2/vpoDN^{29,45}. Although roughly half of the sine-preferring cell types were excitatory (Figure 5C), our screen did not identify any of their downstream targets. As we focused on finding WED/VLP cell types, it is possible that the targets of excitatory sine-preferring neurons have the bulk of their projections in other brain regions. Thus, excitatory pathways for sine processing remain to be further mapped.

To determine whether sine and pulse preference arise early in the pathway (more consistent with model 2), we mapped synaptic connections with 90 JONs previously identified in the EM volume⁴⁶. Since automated synapse detection only identified a handful of JON synapses (see Methods), we instead detected the number of membrane contacts between JONs and auditory neurons (Figure S4B), with the rationale that membranes must be apposed for a synapse to occur (see Methods). We then manually validated the existence and directionality of synapses between JONs and auditory cells (Figure S4D–E). We discovered that 12 central auditory cell types form synapses with JONs, including both inhibitory and excitatory neurons, and neurons from all song preference classes (Figure 5I–J). This demonstrates that song mode preferences can arise early in the pathway, inconsistent with model 1. Four of these cell types were both pre- and postsynaptic to JONs (Figure 5J, Figure S4C–D), three of which are inhibitory, demonstrating that JONs receive feedback inhibition. One cell type (SAD_pr02) appeared to only be presynaptic to JONs (Figure 5J), though its neurotransmitter remains inconclusive. Overall, these findings are consistent with reports of both pre- and postsynaptic sites on JONs⁴⁶.

Taken together, our functional and anatomical results support a novel network organization for auditory processing: sine and pulse preference arise early in the pathway, and synaptic connections between differently tuned cells contribute to generating a continuum of song mode preferences (Figure 3C).

The auditory connectome is non-hierarchical, but nonetheless song responses are predictable from the wiring diagram

We found little evidence of hierarchical organization at a purely structural level. Using the binarized neural connectivity matrix with a threshold of at least 10 synapses between neurons (Figure S4A), we computed three measures of network hierarchy: orderability, feedforwardness, and treeness (Fig 6A). These metrics evaluate the fraction of neurons belonging to network cycles (or recurrent loops in the network), the overall contribution of cycles to paths through the network, and the extent to which the network diverges (fans out) from a set of root nodes, respectively⁴⁷. While the network could be condensed into a feedforward network of connected components (Figure 6B), with approximately half of the neurons uniquely orderable (Figure 6C), paths through the network were nonetheless dominated by recurrent connections, and the network tended to neither fan out nor converge from a set of root neurons. The network deviated only marginally in each metric from random networks with matched degree distributions (Figure 6C–E), with values markedly

less than those of a perfectly feedforward, tree-like network. Thus, the network structure, even when not considering song mode preferences, exhibits little hierarchical organization beyond that expected from chance.

Despite a lack of hierarchical organization, are the responses of individual cell types predictable from their inputs? To address this question, for each neuron belonging to a cell type we imaged, we compared its recorded responses to those predicted by a linear dynamical system model^{48,49} (see Methods) whose inputs were the responses of its presynaptic partners, weighted by their synaptic strengths (Figure 6F–H, K–M). In this model, the time derivative of the response at each time point is given by the connectome-weighted sum of the presynaptic neurons' responses plus a "leak" term that causes the response to decay to zero absent further presynaptic inputs. The model for each neuron is parameterized only by the time constant τ , which determines the decay/leak rate of the postsynaptic response. Since we did not have access to the true membrane time constants, we set $\tau = 0.5$ s for all cells, which roughly recapitulated the observed rise times in the recorded cells (Figure 6H,M).

We computed interpulse interval (IPI or pulse rate) and sine frequency tuning curves of the model responses and compared them to the true tuning curves (Figure 6I–J, N–O). While several neurons' tuning could be predicted well (Figure 6F–O), this varied across neurons (Figure 6P–Q). This may be due to missing inputs in the model, consistent with our observation that IPI and sine frequency tuning prediction errors were strongly correlated (Figure 6R). Additional causes of mismatches between model predictions and data include nonlinear relationships between synapse number and connection strength, nonlinear transformations of synaptic inputs, and/or response heterogeneity within cell type. Nonetheless, the mean prediction error across the population was significantly less than when we randomly shuffled the predictions relative to true tuning curves (Figure 6S–T). This suggests that even absent recordings from all input neurons and a model of variation in intracellular properties, the connectome meaningfully constrains how the tuning of individual neurons emerges from their inputs.

Evaluation of song response timescales

In addition to diversity in song mode preference, our recordings revealed a diversity of response timescales (Figure 3A, 4A). To quantify this, we computed response and adaptation time constants τ_r and τ_a , respectively, by fitting each neuron's pulse and sine responses with a simple model (Figure 7A; note that these are different time constants from those used to predict neural responses from presynaptic inputs in the previous section, as τ_r and τ_a here reflect neural responses to song rather than presynaptic inputs). Response time constants across all recordings were well matched to the duration of male song bouts during natural behavior¹⁵ (Figure 7B), suggesting that the time constants of neural responses are appropriate for analyzing song. Sine song tends to occur in longer contiguous segments than pulse song (Figure 7C), and accordingly, sine-preferring neurons tended to have longer response time constants than pulse-preferring neurons (Figure 7D). Across song mode preference categories, we observed a wide range of response time constants (Figure 7E) and adaptation rates ($1/\tau_a$) (Figure 7F). Although we found no correlation between these

temporal features and pulse vs. sine preferences, we found that stronger preferences for song (compared to noise) were correlated with faster τ_r (Spearman rank correlation, $\rho=-0.31$, $p<0.001$) (Figure 7G) and faster adaptation rates ($\rho=0.35$, $p<0.0001$) (Figure 7H).

To determine whether response timescales may be inherited from a neuron's inputs, we compared the differences in response time constants and adaptation rates between every pair of neurons with the path length between each pair, which is the number of synaptically connected neurons between them. For instance, the path length between a pre- and postsynaptic pair is 1. We found no correlation between the similarity of τ_r and path length (Figure 7I), and only a weak correlation between the similarity of adaptation rate and path length (Spearman $\rho=0.24$, $p<1e-9$) (Figure 7J), suggesting that cell-intrinsic, rather than network properties, play the larger role in shaping response time constants. We posit that the diversity of time constants may be important for processing multi-timescale song structure (see Discussion).

DISCUSSION

Here we identified several new auditory neuron types in the *Drosophila* brain. Prior work had focused on either early or higher-order auditory neurons, leaving open the characterization of intermediate cell types. By systematically characterizing tuning for the two modes of courtship song and examining synaptic connectivity among all new and previously identified auditory neurons using the connectomic resource FlyWire, we discovered extensive interconnectivity between cell classes with different song mode preferences (Figure 5). We found that song mode preference arises in neurons postsynaptic to auditory receptor neurons, and that the connectome lacks hierarchical structure. These results rule out a model in which the two main song modes are processed in separate pathways (and one in which song mode preference is built up within each pathway), but instead support a model in which interconnectivity contributes to generating a continuum of song mode preferences. We tested this by predicting responses at each node in the connectome from the responses of the inputs using a simple linear model (Figure 6), and discovered strong predictability, suggesting that the wiring diagram places a strong constraint on functional responses, consistent with recent studies in the fly olfactory system⁵⁰.

Response continuums have been observed in fish^{51,52} and rodents^{53 54 55}, and are thought to support more efficient encoding than would be possible with categorical representations. In the fly auditory system, neurons with intermediate preference (that respond roughly equally to sine and pulse) could encode sound intensity, location, and/or long timescale features, such as the variable sequence of pulses and sines that make up song bouts¹⁵. The continuum of song preferences we discovered among WED/VLP neurons matches that found throughout the entire brain (Figure 3), suggesting that these neurons are representative of the larger auditory population, including those neurons that drive song-responsive behaviors. Many descending neurons (DNs) that control locomotion have dendrites in a number of regions with auditory activity, including WED/VLP^{56,57}. Sampling from a continuum of responses to sine and pulse would provide these DNs with the ability to respond to a wide array of song patterns. Finally, we also found a continuum of time

constants among auditory neurons (Figure 7). This diversity of timescales matches the distribution found in natural song bouts, and female behavior is sensitive to song history across timescales¹⁷. The diversity of neural response time constants could serve as a useful substrate for retaining the multi-timescale structure of song history in a population neural code.

We identified new auditory neurons by targeting cells within the WED/VLP, putative auditory areas^{25,32}. In the connectome we built using FlyWire³¹, which allows proofreading of EM reconstructions in an entire female brain³⁹, we could examine inter-hemispheric connections, as well as ipsilateral vs. contralateral connection patterns (Figure 5H).⁵⁸ By combining functional and connectomic data, we could predict auditory tuning from the wiring diagram, and our findings reveal the importance of the connectome for understanding sensory responses. How many neurons remain unknown in the auditory pathway is difficult to estimate, but continued EM circuit tracing combined with functional imaging of sparse driver lines, as we did here, should ultimately fill out the auditory connectome. Since song representations are present in 33/36 central brain areas²¹, we expect auditory circuits to be highly interconnected to circuits of other modalities and functions. Indeed, the auditory neurons we discovered send projections throughout the brain, including to olfactory, visual, and pre-motor areas (Figure S2), suggesting roles in multisensory integration.

Prior pan-neuronal imaging work found tonotopy in JON axons that was maintained in the AMMC and potentially sharpened in the WED²⁰. Here we uncovered that neurons directly downstream of the JONs exhibit strong preferences for pulse or sine song (Figure 5I–J), suggesting that such preferences may be inherited from the periphery. We also found that multiple cell types provide inhibitory feedback onto JONs (Figure 5I–J). In vertebrates, efferent inhibition protects against damage from loud sounds by modulating the sensitivity and selectivity of the auditory periphery⁵⁹. Whether any of the connections we describe here play a similar role remains to be determined. Very few WED/VLP neurons showed band-pass tuning for conspecific pulse rate, suggesting that downstream processing generates such selectivity, as is observed in neurons such as pC2I or vpoEN^{16,28,29}. For instance, the two inputs onto vpoEN with the most synapses are inhibition from AVLPr01 and excitation from WED-VLP (Figure 5H), both of which respond most strongly to short IPIs (Figure 4B). This pattern could result in band-pass tuning in vpoEN since the inhibition is sharply tuned to IPIs shorter than the conspecific range, allowing excitation to dominate in the conspecific range. This would be consistent with vertebrate auditory systems, in which frequency tuning arises in the periphery, whereas tuning for temporal features, such as pulse rate, arises through central computations⁶⁰. We also found that the responses of some cell types were highly stereotyped across animals, whereas others were more variable. The role of variability in auditory responses is currently unknown, but it may function to generate variation in song preference across animals, potentially useful for diversifying female mate selection preferences.

Mapping synaptic connectivity among auditory neurons revealed a high degree of intermixing between preferences for the two song modes (Figure 5H). One example is inhibitory interactions that refine tuning. For instance, the three sine-preferring inhibitory

cell types we described (GNG_pr01, AVLP_pr01, and AVLP_pr02) all send outputs to different pulse-preferring neurons (Figure 5H), suggesting that a major role for these neurons is to enhance or establish pulse preferences. The use of inhibition to sharpen auditory tuning is widespread. In grasshoppers and katydids, convergence of narrowly-tuned inhibition with broadly-tuned excitation shapes frequency tuning^{61,62}. Sideband inhibition, in which stimuli just outside of a neuron's preferred range elicit inhibition, also sharpens frequency tuning in mammalian central neurons⁶³. Inhibitory connections occurred between almost every possible combination of song-mode preference classes (Figure S5G), suggesting that inhibition may play a number of roles in shaping song tuning in flies.

Prior work on auditory systems has led to ideas about segregation of processing into separate streams for different sound categories^{64,65}, but these ideas do not address how animals might encode patterns or sequences of sound elements. Further, while separate streams may be useful for detecting different classes of stereotyped acoustic signals, such segregation may not be sufficient for analyzing rapidly varying sequences of elements, as occur in fly and some types of bird songs^{15,66}. In these cases, encoding longer timescale patterns, such as the recent history of interleaved song modes, may benefit from drawing upon neural responses with a range of auditory preferences. Future work should examine how this network is read out by downstream neurons to drive behavioral responses to song.

STAR METHODS

Resource availability

Lead contact.—Further information and requests for resources and reagents should be directed to and will be fulfilled by the lead contact, Mala Murthy (mmurthy@princeton.edu).

Materials availability.—Split-GAL4 lines generated by this study are available from Janelia.

Data and code availability.—Raw data supporting the current study are publicly available: <https://doi.org/10.34770/7zem-x425>. Code generated by the current study is also publicly available: https://github.com/rkp8000/7UN3_1N_DROP_OU7. Any additional information required to reanalyze the data reported in this paper is available from the Lead Contact upon request.

Experimental model and subject details.

The split-GAL4 system^{68,69} was used to express the activation domain (AD) and the DNA-binding domain (DBD) of GAL4 under the separate control of two genomic enhancers, to obtain the intersection of their expression patterns, with the goal of obtaining a sparser pattern. Split-GAL4 stocks were gifts of Gerald Rubin and Barry Dickson^{69–71}. 20xUAS-GCaMP6s, td-Tomato/CyO was generated by Diego Pacheco²¹. The genotype of imaged flies was 20xUAS-GCaMP6s, td-Tomato/GAL4-AD; GAL4-DBD/+, with the “+” originating from NM91 stocks. For expression pattern staining, split-GAL4s were combined with 20xUAS-CsChrimson-mVenus trafficked in attP18, except that 6 lines (17963, 21914,

23281, 23627, 28822, 29146) were shared from a different project that instead used pJFRC51–3XUAS-IVS-syt::smHA in su(Hw)attP1, pJFRC225–5XUAS-IVS-myr::smFLAG in VK00005, and one (27932) used pJFRC200–10XUAS-IVS-myr::smGFP-HA in attP18, pJFRC216–13XLexAop2-IVS-myr::smGFP-V5 in su(Hw)attP8. For multicolor flip-out (MCFO) staining, all were crossed to MCFO-1 [pBPhsFlp2::PEST (attP3);; pJFRC201–10XUAS-FRT>STOP>FRT-myr::smGFP-HA (VK0005), pJFRC240–10XUAS-FRT>STOP>FRT-myr::smGFP-V5-THS-10XUASFRT>STOP>FRT-myr::smGFP-FLAG (su(Hw)attP1)]. Flies were kept at 25C with a 12h:12h light:dark cycle. All experiments were performed on female flies.

Method details.

Split-GAL4 creation.—GAL4 images from the Rubin and Dickson collections^{69,70,72} were visually screened for lines targeting neurons in the WED and AVL. For each cell type, a color depth MIP mask search⁷³ was conducted to find other GAL4 lines with expression in similar cells. Split-GAL4 hemidriviers for these lines were crossed in various combinations to find a combination that targeted the cell type of interest but with sparse expression elsewhere, determined by expression and staining of mVenus in one female fly of genotype 20xUAS-csChrimson::mVenus (attP18)/w; Enhancer-p65ADZp (attP40)/+; Enhancer-ZpGAL4DBD (attP2)/+. 65 combinations were chosen by this method, representing over 50 cell types. In some cases, lines targeting neurons with similar gross morphology revealed one line with a commissure (see SS16374 and SS27885; SS41728 and SS41730 in Data S1A). For these examples, we characterized both lines due to the difficulty in determining whether they were truly similar cell types. Split-GAL4 combinations were then double balanced and combined in the same fly strain to make a stable split-GAL4, for which expression pattern staining was carried out in an additional female to confirm the expression seen in the initial screen. For multiple split-GAL4 lines targeting morphologically similar neurons, one (or sometimes a few) were selected according to the following criteria: least off-target expression in the central brain, largest number of neurons with expression, and/or most reliable calcium responses to acoustic stimuli across flies. Expression was further confirmed in multiple flies by multicolor flip-out staining (see below). All lines generated here and the corresponding image stacks are available via <https://splitgal4.janelia.org>.

CNS immunohistochemistry & imaging.—Brains and ventral nervous systems were dissected and stained using published methods^{74–76}. Antibodies used were rabbit anti-GFP (1:500, Invitrogen, #A11122), mouse anti-Bruchpilot (1:50, Developmental Studies Hybridoma Bank, University of Iowa, mAb nc82), Alexa Fluor 488-goat anti-rabbit (1:500, ThermoFisher A11034), and Alexa Fluor 568-goat anti-mouse (1:500, ThermoFisher A11031). Serial optical sections were obtained at 1µm intervals on a Zeiss 700 confocal with a Plan-Apochromat 20x/0.8NA objective. A detailed description of the staining and screening protocol is available at <https://www.janelia.org/project-team/flylight/protocols> under “IHC - Adult Split Screen.”

Stochastic labeling.—For multicolor flip-out (MCFO) stochastic labeling⁷⁴, approximately 8 females per split-GAL4 line received a 15 min heat shock at 37°C at 1–3

days old, and were dissected at 6–8 days. A detailed description of the MCFO protocol can be found at <https://www.janelia.org/project-team/flylight/protocols> under “IHC - MCFO.”

Image processing.—Images were adjusted for brightness and contrast without obscuring data. Images were processed in ImageJ (<https://imagej.nih.gov/ij/>) and Photoshop (Adobe Systems Inc.). Where noted, neurons were rendered and segmented from confocal stacks with VVDviewer software (https://github.com/takashi310/VVD_Viewer)^{77,78} to visualize them in isolation. For this rendering and for computational alignment of brain images used where noted, brain images were registered using the Computational Morphometry Toolkit⁷⁹ to a standard brain template (“JFRC2014”) that was mounted and imaged with the same conditions. Segmented image stacks are available at <https://splitgal4.janelia.org>.

Neuropil innervation.—We registered the neuropil⁸⁰ maps to the unisex JRC2018 template by first bridging from IBNWB to JFRC2⁸¹, and then JFRC2 to unisex JRC2018⁸². To determine which neuropils each neuron type targeted, we used the segmented neuron stacks with manually removed somata. We then calculated the percentage of the neuron’s voxels in each neuropil. In Figure S2 we report all neuropils containing at least 1% of each segmented neuron’s total volume.

For naming auditory neurons not previously described as auditory, we used the neuropil in which the segmented neuron had the greatest percentage of expression. If a neuron had nearly equal (<1% difference) expression in two neuropils, we used both neuropil names. A two digit number was added to the neuropil name in sequential order based on the split-GAL4 line number (Table S2). To disambiguate our names from those of the hemibrain project⁸³ (as our neuron types/cell classes can likely be further segregated into subtypes based on both morphological and connectivity differences within a line), we added a ‘pr’ before each number for Princeton.

EM reconstructions.—We identified individual neurons in the FAFB volume using FlyWire.ai³¹. Neurons were proofread using the editing tools in FlyWire to add missing pieces of arbor and remove incorrect pieces, focusing on the main backbone of a neuron, not attempting to add very small missing twigs. Sister cells from the same cell type were used to verify that a cell’s overall morphology appeared generally correct. WED/VLP reconstructions were proofread by 12 proofreaders consisting of both scientists and expert tracers from the Seung and Murthy labs. To find all candidates belonging to a given cell type, we found an EM cross-section of the primary neurite tract, and investigated every cell in the cross-section. We compared candidate reconstructions with LM images of our auditory lines (Data S1A–C). We were conservative with which reconstructions we included for each cell type; if a reconstruction did not match neurons present in MCFO images (Data S1B), we excluded it. Since a limited number of MCFO images were available for each line, it is possible that we may have missed some EM reconstructions belonging to each line. Two auditory cell types (AVLP_pr18 and AVLP_pr24) did not have enough cell-type resolution in MCFO to enable individual EM reconstruction identification and were excluded from the synaptic connectivity mapping. EM reconstructions for pC1a/d/e, pMN1/DNp13, and pMN2/vpoDN came from a previous study⁸⁴. We identified vpoEN and vpoIN by inspecting the inputs to pMN2/vpoDN neurons²⁹. pC2l reconstructions were

identified by D. Deutsch (personal communication). A list of all auditory neurons identified in FlyWire, along with their FlyWire coordinates and root ID numbers are listed in Table S3.

There are just under 60 B1 neurons per hemisphere³¹, yet our split-GAL4 line targeting B1 neurons labels just a handful. Therefore, to determine which B1 subtypes our split-GAL4 line labeled, we compared MCFO images (Data S1B) to EM reconstructions³¹ and estimated that our split-GAL4 line contains a mix of B1–1-3 subtypes.

Synaptic connectivity among auditory neurons.—We used FAFB reconstructions corresponding to previously known auditory neurons³¹, higher-order auditory neurons^{29,84}, and all auditory WED/VLP neurons for which we found EM reconstructions. We then found all automatically detected synapses between every pair of individual neurons⁴¹, using version 11 of the FlyWire synapse table (3rd column of Table S3). We omitted synapses that may have been identified multiple times by eliminating synapses between a given pair for which the presynaptic site was within 150 μm of another presynaptic site. We ignored synapses from one neuron onto itself and between individual neurons of the same cell type, due to the high rate of false positives in these cases³¹. To generate connectivity diagrams based on cell types, we normalized the total number of synapses between two cell types by the number of postsynaptic neurons, and show all such connections that exceed 10 synapses/postsynaptic neuron. Applying our criteria to early auditory neurons results in the same connectivity results among the neurons in³¹, with one exception. Dorkenwald and colleagues found that one automatically indicated connection between cell types was due to a high number of inverted synapses (ie, automatically detected presynaptic partner was determined to be postsynaptic by a human observer)³¹. Our connectivity analysis method is unable to confirm synapse directionality, and it is not yet known how often this type of false positive occurs. Five WED/VLP cells (AVLP/PVLP_pr01, AVLP_pr05, AVLP_pr35, IPS_pr02, and IPS/WED_pr01) did not have connections meeting these criteria with any other cell type in our dataset.

A previous study identified 5 subtypes of the B1 neurons (B1–1-4 and B1-u for unidentified) based on connectivity patterns³¹. Here we find evidence within B1-u of a 6th subtype we name B1–5. These neurons are distinct from the rest of the B1-u neurons as they have significant outputs onto WED_pr01 and WED_pr02 (Figure S4A).

Contacts between JONs and auditory neurons.—In FlyWire, we proofread the JONs previously identified by Kim and colleagues⁴⁶. To map connectivity with auditory neurons, we counted the automatically detected synapses⁴³ between JONs and auditory neurons using version 274 of the FlyWire synapse table (root ID numbers given in column 4 of Table S3), but found that there were a large number of false negatives compared to previous reports⁴⁶. Since the synapse detection algorithm was not trained on JON synapses⁴³, our results suggest that JON synapses may contain unique morphology at or near the synapse compared to central brain neurons. Therefore, we used the number of contacts between JONs and auditory neurons as a measurement of the number of potential synaptic connections, with the rationale that membranes need to touch for a synapse to occur, but that membrane contact does not ensure synaptic connectivity. We found contacts between neurons by analyzing the PyChunkedGraph representation of the segmentation³¹. In the

PyChunkedGraph, larger segments are broken down into small segments called supervoxels. All supervoxels are nodes in the supervoxel graph and each touching pair of supervoxels has an edge between them. Edges between supervoxels belonging to the same cell segment are “active” and edges between supervoxels belonging to different cell segments are “inactive”. Therefore, inactive edges in this graph represent contacts between cell segments. To find all contacts between every pair of cell segments, we first identified the inactive supervoxel edges between them. Then, we built a subgraph of all involved supervoxels and all their edges. Finally, we found all contacts by computing the connected components in this subgraph. We compared our membrane contact counts (Figure S4B) to the number of manually quantified synapses for the subset of neurons that appeared in ⁴⁶, and found a linear relationship with slope near 1 ($y = 0.84x + 0.40$, $R^2 = 0.90$) (Figure S4C). Therefore, we used the number of contacts between JONs and auditory neurons as a measurement of the number of potential synaptic connections. For every pair of cell-type to cell-type connection ($n=19$) indicated by our membrane contact analysis, we manually verified the existence and directionality of synapses between two randomly selected individual neurons with at least 10 contacts between them. This led us to verify 11 connections in which JONs were presynaptic, 4 connections in which JONs were both pre- and postsynaptic, and 3 connections in which JONs were only postsynaptic (Figure 5I–J); and to exclude 1 connection in which we found only 1 synapse.

Path length measurement.—We used the synaptic connectivity matrix (Figure S4A) to define a graph with directed edges. We then calculated the shortest path between every pair of neurons while ignoring edge weights, and then averaged within cell types.

Analysis of hierarchical network structure.—We binarized the connection matrix between individual neuron pairs (Figure S4A), keeping only connections where at least 10 synapses between the two neurons had been detected in the connectomic analysis, and then computed orderability, feedforwardness, and treeness of the resulting directed binary network G , as described in ⁴⁷. We first computed the “node-weighted condensed graph,” or graph condensation, G_C (Figure 6B) of the original network by identifying all strongly connected components $\{v_j\}$ of G (sets of neurons all mutually reachable from one another via at least one directed path) and retaining whether or not at least one directed connection existed between each pair of components. Thus, G_C is a directed, acyclic (no recurrent loops) graph whose nodes are the strongly connected components of G . Any neurons that were not connected to the dominant network were left out of our calculations.

Orderability was calculated as the fraction of neurons that were not included within any recurrent loop in G (i.e. the number of neurons that were their own strongly connected component of size 1, divided by the total number of neurons). Feedforwardness was calculated by examining each path in G_C that emanated from a “starting node” (a node with no incoming connections) and finished at an “ending node” (a node with no outgoing connections), dividing the number of nodes in that path by the total number of neurons represented by those nodes, then averaging this ratio over all paths from starting to ending nodes. Treeness was calculated by (1) calculating the forward path entropy $h_f(v_j)$ of each starting node v_j in G_C , (2) computing H_f , the mean forward path entropy over all starting

nodes, (3) calculating the backward path entropy $h_b(u_i)$ of each ending node u_i in G_C , (4) computing H_b , the mean backward path entropy over all ending nodes, and (5) taking the normalized difference between the mean forward and backward path entropies, with the final feedforwardness given by $(H_f - H_b)/\max(H_f, H_b)$. The forward path entropy of a starting node is the entropy of all paths emanating from that node and finishing at any ending node, $h(v_j) = -\sum_{\text{path}} P(\text{path}) \log_2 P(\text{path})$ where $P(\text{path})$ is the probability of taking a given path by starting at v_j and repeatedly stepping to a downstream node (selecting uniformly at random among all possible downstream nodes) until an ending node is reached. The backward path entropy of an ending node, $h(u_i)$, is the equivalent quantity, but starting from the ending node and traversing the network backwards until a starting node is reached. See ⁴⁷ for further mathematical details.

Fully random networks were generated using the same number of neurons as the empirical network and assigning connections at random with the same connection probability as measured empirically. Degree-constrained random networks were generated by fixing the number of incoming and outgoing connections of each neuron in the random network to match those of a corresponding neuron in the empirical network (with 1-to-1 correspondence), but otherwise assigning connections between neuron pairs at random.

Neurotransmitter predictions.—We predicted the neurotransmitter for 479 neurons within 48 cell types using the method presented in ⁴². We used FlyWire ³¹ to retrieve all automatically detected pre-synaptic sites in each neuron segment and filtered out synapses with a cleft score below 50 to remove likely false positives ⁴³. We predicted the neurotransmitter of each pre-synaptic site individually and defined the neurotransmitter of an entire neuron as the predicted majority neurotransmitter over its synapses. We labeled a neuron as inconclusive if its majority transmitter was predicted for less than 65% of its synapses. Using this cutoff leads to a greater than 95% prediction accuracy for the three fast-acting neurotransmitters GABA, acetylcholine and glutamate on the test set presented in ⁴² (see Figure S5A). We validated whether neurotransmitter predictions from automatically detected pre-synaptic sites were robust by predicting the neurotransmitter of neurons within 6 auditory cell types with known neurotransmitters and found perfect agreement for all neurons with conclusive neurotransmitter predictions (Figure S5B). Neurotransmitter predictions for all cell types are shown in Figure S5B–C.

The classifier predictions for all but 5 cell types (pMN2/vpoDN, SAD_pr02, AVLPr04, A1, and SAD_pr01) agreed for at least 60% of individual neurons in each class. Therefore, we did not assign a neurotransmitter identity to these cell classes. The one exception was AVLPr04, in which we found evidence for multiple cell types. MCFO results revealed that the split-GAL4 line labeling AVLPr04 consisted of two cells per hemisphere, both with diffuse and widespread branching patterns across the AVLPr04 and PVLPr04, but with one cell type having a projection toward the midline (Data S1B). We identified EM reconstructions matching both these cell types and included them as AVLPr04 (Figure 2). The cells with the midline projection in both hemispheres were predicted to be dopaminergic (Figure S5C), whereas the two remaining cells were predicted to be GABAergic or glutamatergic. We also found that synaptic connectivity was different for the dopaminergic vs. non-dopaminergic

cells (Figure 5H). Therefore, we conclude that AVLP_pr04 contains one dopaminergic cell per hemisphere and one additional cell with inconclusive neurotransmitter results.

Calcium imaging.—We used GCaMP6s³⁴ to maximize the signal to noise of our recordings and thus increase the likelihood that we could observe even weak auditory responses. For calcium imaging experiments, we used 3–11 day-old virgin female flies reared at 25C and housed in groups of 1–8 flies/vial after eclosion. Calcium imaging experiments were performed during the fly's light cycle. Flies were mounted and dissected as described in⁸⁵ with the following modifications. Before mounting the fly, we removed the wings and legs with forceps. We removed fat covering the brain with forceps or with mouth suction through a sharp glass pipette. We ensured the arista were intact and free by gently blowing on the fly before and after each experiment. We also looked for abdominal contractions in response to gentle blowing to indicate the fly was alive and healthy before and after each experiment. We monitored temperature and humidity with a thermometer and hygroscope (Traceable 15–077-963, Webster TX) placed on the air table with the two-photon microscope. Temperature and humidity were stable within an experiment, with fluctuations of <1C and <5% humidity across 8 hours of imaging (~1 fly/hr).

Imaging was performed as previously described¹⁶. Briefly, we used a custom-built two-photon laser scanning microscope controlled in MATLAB by ScanImage 5.1 (Vidrio). We imaged single planes at 8.5 Hz (256 × 256 pixels). Pixel size was 0.75 μm × 0.75 μm. After dissection, a fly was placed under the microscope with continuous saline perfusion delivered to the meniscus.

ROI selection.—To decide which region of interest (ROI) to record from in each neuron, we first sampled from multiple ROIs, depending on the morphology of the neuron and on the level of baseline GCaMP6s expression (ie, only ROIs with some baseline level of GCaMP expression were visible under the two-photon microscope). In some lines, multiple ROIs were visible and responded relatively robustly. In those cases, we narrowed down which ROI to focus on based on response strength and ability to locate roughly the same ROI across flies. In other lines, baseline GCaMP expression was low, so we imaged from the ROI that was visible within a moderate laser power, with the goal of choosing roughly a similar ROI in each fly. We sampled from both the left and the right hemisphere within each line but from different flies. In all of the lines, responses occurred in both hemispheres, suggesting either that we stimulated both arista or that ROIs at the level of the WED/VLP respond bilaterally.

Stimulus generation and delivery.—Sound stimuli were generated at a sampling frequency of 10kHz using custom MATLAB software and previously published techniques¹⁶. Sound was delivered through an earbud speaker (Koss, 16 Ohm impedance; sensitivity, 112 dB SPL/1 mW), which was attached to a long thin tube (12cm, diameter: 1mm) placed ~2mm from the fly's head (directed toward the arista) and controlled by custom software in MATLAB⁸⁶. Sound intensity was calibrated by measuring the sound particle velocity component for a range of frequencies (100–800 Hz). The detailed procedures and cross-calibration between the pressure and the pressure gradient microphone were described in⁸⁷. To estimate the sound amplitude of each stimulus we placed the calibrated gradient

microphone at the same position as the fly (2–3 mm from sound tube outlet) in separate experiments. The recorded voltage was then converted to particle velocity (with units mm/s). The output signal was corrected according to the measured intensities to ensure equivalent intensity across frequencies, as previously described ²².

To characterize a given neuron type as auditory or non-auditory, we used a stimulus set consisting of pulse song, sine song, and broadband noise, each with 10 sec duration and 10 sec pre- and post-stimulus silent periods. The intensity of pulse and sine stimuli was 5 mm/sec and the intensity of the noise stimulus was 2 mm/sec. To further characterize auditory tuning, we used a stimulus set consisting of 5 pure tones at a range of frequencies (100, 200, 300, 500, and 800 Hz) and 5 pulse stimuli with a range of interpulse intervals (16, 36, 56, 79, and 96 ms), all at an intensity of 4 mm/sec. Each of these stimuli were 4 sec in duration, with 5 sec pre-stimulus and 10 sec post-stimulus silent periods. Within a stimulus set, a block was defined as one presentation of each stimulus. Stimulus order was randomized within each block, and 3–7 blocks were presented to each fly.

Analysis.—Data were analyzed using custom software in MATLAB. ROIs were drawn manually based on a z-projection of the td-Tomato signal. We calculated the mean fluorescence within each ROI frame-by-frame. If any stimulus block contained drastic, brief (1–3 sec) increases in fluorescence, indicative of wax or other particles moving into the imaged region, we discarded the entire block. We used only flies in which 3 or more blocks were available for analysis. We corrected for gradual, modest changes in fluorescence during each recording by de-trending the data. To detrend, we concatenated fluorescence traces over an entire recording, used a running percentile filter (20th percentile, 50 sec window, 5 sec shift), and subtracted this long-term trend from the recording. For each stimulus, we calculated dF/F as $(F(t)-F_0)/F_0$, where F_0 was defined as the mean fluorescence during the 10 sec prestimulus silent period.

Stimulus modulation of calcium signals.—To determine whether the fluorescence within a given ROI was modulated by at least one of the acoustic stimuli, we followed the method previously described in ²¹. Briefly, we modeled the GCaMP fluorescence trace as a convolution of the stimulus history and a set of filters, one per stimulus (ie, 3 filters for the screen stimuli and 10 filters for the frequency/IPI tuning stimuli), with the filter duration matching the duration of the stimulus. To estimate each filter, we used 80% of the stimulus repetitions as training data and the remaining 20% of the repetitions as test data. Filters were estimated using ridge regression ⁸⁸. We convolved the estimated filters with the stimulus history to generate the predicted signal for each ROI. All possible combinations of training and test data repetitions were used, which gave a total of 3–15 predicted signals (3–6 total repetitions, respectively) per ROI. We then measured the Pearson correlation coefficient between the raw (ie, test repetitions) and the predicted signals. We used bootstrapping to determine the statistical significance of the resulting correlation coefficients. We randomly shuffled each test fluorescence trace in 10 sec bins, and then calculated the Pearson correlation coefficient between each of 10,000 independently shuffled test signals and the predicted signal. P-values for the correlation coefficients were defined as the fraction of shuffled correlation coefficients > 30th percentile of the estimated correlation coefficients.

P-values were corrected for multiple comparisons with the Benjamini-Hochberg procedure, with a false detection rate of 0.05.

Analysis of auditory responses.—We measured the strength of calcium responses to auditory stimuli only in ROIs which we determined to be statistically modulated by the stimuli. In these cases, we calculated the integral of the dF/F signal starting with stimulus onset and ending 4 sec after stimulus offset, and then divided by the total time of the integral window. We set out to image auditory responses from at least 4 flies per cell type. If the percentage of responding flies fell below 15%, we labeled that cell type as an infrequent responder and stopped pursuing recordings from that cell type. We chose the threshold of 15% for defining auditory vs. infrequent responders based on the practicality of pursuing recordings from cells that did not respond reliably. Since we set out to image from multiple flies from the same line, achieving this goal would require many more recordings from cells that respond in only 15% of flies. If no flies from a given cell type responded to acoustic stimuli (out of at least 4 imaged flies), we characterized the cell type as non-auditory.

To quantify within-fly variability, we concatenated z-scored responses to pulse, sine, and noise and then measured the standard deviation. To quantify across-fly variability, we measured the standard deviation between the average z-scored responses for all recordings from a given split-GAL4 line.

We used the integrals elicited by pulse, sine, and noise stimuli to assess each fly's song vs. noise preference. For each fly, we defined the response to song as the maximum of the integrals in response to pulse and sine. We then calculated a song vs. noise preference index as $(\text{song} - \text{noise}) / (\text{song} + \text{noise})$ after setting all negative integrals to 0. Ignoring instances of net inhibition (ie, negative integrals) allows us to quantify the stimuli that excite a given cell type while limiting the preference index to between -1 and 1 . If both integrals were negative, we set the song mode preference to 0 to indicate that the response did not prefer either stimulus. We calculated a song mode preference index as $(\text{pulse} - \text{sine}) / (\text{pulse} + \text{sine})$ after setting all negative integrals to 0. If both integrals were negative, reflective of net inhibition to both stimuli, we set the song mode preference to 0 to indicate that the response did not prefer either stimulus. Next we reasoned that in a pulse-preferring neuron, the pulse integral should be at least 250% of the sine integral, which corresponds to a preference index of 0.43 (Figure 3C). Likewise, we required a sine-preferring neuron to have a sine response that was at least 250% of the pulse integral, which corresponds to a preference index of -0.43 . To classify the preference of each cell type, we used the mean preference index across flies. Neurons with a mean preference index between -0.43 and 0.43 were classified as having intermediate preference. We chose the threshold of 250% because it best captured trends in the data. That is, pulse- and sine-selective neurons defined by this threshold had individual fly responses that were almost exclusively pulse- or sine-selective, respectively (Figure 3C). To quantify the stimulus preference of net inhibition (ie, negative integrals), we again calculated a sine vs. pulse preference index after setting all positive integrals to 0. This allowed us to determine which stimulus elicited stronger inhibition.

For principal components analysis (PCA), we measured the integrals of z-scored dF/F traces starting with stimulus onset and ending 4 sec after stimulus offset. Each observation

consisted of the integrals evoked by the IPI and frequency tuning stimuli from one recording.

Tuning curve generation and classification.—To generate frequency and interpulse interval tuning curves, we measured the integrals in response to each stimulus. Next we classified frequency and interpulse interval tuning curve types based on previously published methods^{89,90}. Briefly, if the minimum tuning curve value was >85% of the maximum tuning curve value, we classified the tuning as all-pass (ie, untuned to the tested stimulus parameter). For all other tuning curves, we fit both a sigmoid and a Gaussian function. If the r^2 of both the sigmoid and Gaussian fits were <0.5, we classified the tuning as complex. Since high- and low-pass tuning curves can be well fit by both a Gaussian and a sigmoidal curve, we used the $r^2_{\text{sigmoid}}/r^2_{\text{Gaussian}}$ ratio. If $r^2_{\text{sigmoid}}/r^2_{\text{Gaussian}}$ was <0.85, we classified the tuning curve as band-pass if the Gaussian amplitude was positive and band-stop if the Gaussian amplitude was negative. For frequency tuning curves, if $r^2_{\text{sigmoid}}/r^2_{\text{Gaussian}}$ was >0.85, we classified the tuning as high-pass if the ratio of the sigmoid slope to the sigmoid amplitude was positive, and low-pass if this ratio was negative. For IPI tuning curves, if $r^2_{\text{sigmoid}}/r^2_{\text{Gaussian}}$ was >0.85, we classified the tuning as long-pass if the ratio of the sigmoid slope to the sigmoid amplitude was positive, and short-pass if this ratio was negative.

Prediction of tuning from presynaptic inputs.—For each postsynaptic cell j in the connectome for which we had recorded tuning data (i.e. we had recorded calcium responses to 5 IPIs and 5 sine frequencies from the corresponding split-GAL4 line (Figure 4)), we constructed the following model of its response $r_j(t)$ to activity in its presynaptic inputs:

$$\tau \frac{dr_j}{dt} = -r_j + \sum_i w_{ij} r_i(t)$$

where $r_i(t)$ is the activity in the presynaptic neuron i , and w_{ij} is the number of detected synapses from neuron i onto neuron j , multiplied by -1 if the synapses were GABAergic. As we did not have enough electrophysiological constraints to set τ differently across individual neurons, we used $\tau = 0.5$ s for all neurons. Each valid cell could be classified into a cell line whose tuning responses we measured and hence assigned a response $r_j(t)$ to each of the five IPIs and each of the five sine frequencies that were presented. For each IPI or sine frequency, the response timecourses of the presynaptic cells to that IPI or sine frequency, $r_i(t)$, were used as inputs in the model above to produce the model output $r_j(t)$. The result was a true and modeled set of IPI and sine frequency response timecourses for each valid cell, where the modeled responses were derived from the presynaptic responses and the connectome. We zeroed the input weights w_{ij} of presynaptic cells absent from the connectome or for which we did not have tuning data. Postsynaptic tuning curves of the model to IPI or sine frequency were then computed identically as the tuning curves of the real postsynaptic data. To compare tuning curve shape rather than absolute magnitude, we z-scored both the model and data tuning curves before computing the root mean squared error between the tuning curves.

Analysis of neural response timescales.—We estimated the response and adaptation time constants (τ_r and τ_a , respectively; Fig 7A), of all neurons by fitting the following model to each pair of pulse & sine responses:

$$\tau_r \frac{dr}{dt} = -r + (1 - a_s)I_s(t) + (1 - a_p)I_p(t)$$

$$\tau_a \frac{da_s}{dt} = -a_s + I_s(t)$$

$$\tau_a \frac{da_p}{dt} = -a_p + I_p(t)$$

where I_s and I_t represent sine and pulse inputs (equal to 1 when the corresponding stimulus is on and 0 otherwise), and a_s and a_p are multiplicative adaptation variables for the sine and pulse stimuli, respectively. For each neuron we fit the parameters τ_r , τ_a , a_s , a_p that minimized the time-averaged squared difference between the model response $r(t)$ and the recorded response, averaged across sine and pulse stimuli. We define the adaptation rate as $1/\tau_a$. Since we used the slow calcium sensor, we may slightly overestimate these time constants due to the slower kinetics of GCaMP6s.

Quantification and statistical analysis

Since the majority of our data were not normally distributed according to Jarque-Bera tests, we used non-parametric tests throughout. Correlation tests were based on Spearman's rank correlation (Figure 3 and 7) in Matlab and Wald test (Figure 6) in Python. Details on each statistical analysis including exact values of n , what n represents, and definition of center can be found in the figure legends and Results.

Supplementary Material

Refer to Web version on PubMed Central for supplementary material.

ACKNOWLEDGEMENTS

We thank Xiao-Juan Guan for help with crosses during split-GAL4 generation; David Deutsch for help with calcium imaging pre-analysis and for identifying pC21 neurons in FlyWire; Sebastian Seung for assistance with FlyWire infrastructure; Greg Jefferis for feedback on the cell type naming scheme and Alex Bates and Greg Jefferis for helpful discussions and ideas with regard to neurotransmitter analysis; Nat Tabris and Arie Matsliah for help with connectivity analysis; Lucas Encarnacion-Rivera, Ben Silverman, Jay Gager, Merlin Moore, Selden Koolman, James Hebditch, Sarah Morejohn, Kyle Willie, Austin Burke, Celia David, Ryan Willie, Sandeep Kumar, Doug Bland, Shirleyjoy Serona, J. Anthony Ocho, Nash Hadjerol, Zhihao Zheng, Szi-chieh Yu, Stefanie Hampel, Lucia Kmecova, Fernando J Figueroa Santiago, Fabianna Szorenyi, Yijie Yin, Imaan Tamimi, Varun Sane, Siqi Fang, Griffin Badalemente, Laia Serratos Capdevila, Greg Jefferis, Katharina Eichler, Alexander Bates, Irene Salgarella, Marlon Blanquart, A. Javier, Arti Yadav, Joseph Hsu, and Kyle Thieringer for proofreading FlyWire neurons; Marta Costa, Jan Clemens, and Istvan Taisz for comments on the manuscript; and the Janelia Fly Core, FlyLight, and Scientific Computing groups. A.N. thanks Gerry Rubin, in whose lab he performed this work, for his support and encouragement. We acknowledge funding from the Jane Coffin Childs Foundation (to CAB), NIH NINDS DP2 New Innovator Award and HHMI Faculty Scholar Award (to MM), NIH BRAIN Initiative R01 MH117815-01 (to CM, SD, and MM), and the Howard Hughes Medical Institute (to CM, AN, NE, JF, and BJD).

REFERENCES

1. Akre KL, Farris HE, Lea AM, Page RA, and Ryan MJ (2011). Signal perception in frogs and bats and the evolution of mating signals. *Science* 333, 751–752. [PubMed: 21817052]
2. Baker CA, Clemens J, and Murthy M (2019). Acoustic Pattern Recognition and Courtship Songs: Insights from Insects. *Annu. Rev. Neurosci.* 42, 129–147. [PubMed: 30786225]
3. Hedwig BG (2016). Sequential Filtering Processes Shape Feature Detection in Crickets: A Framework for Song Pattern Recognition. *Front. Physiol.* 7, 46. [PubMed: 26941647]
4. Nieder A, and Mooney R (2020). The neurobiology of innate, volitional and learned vocalizations in mammals and birds. *Philos. Trans. R. Soc. Lond. B Biol. Sci.* 375, 20190054. [PubMed: 31735150]
5. Behr O, and von Helversen O (2004). Bat serenades—complex courtship songs of the sac-winged bat (*Saccopteryx bilineata*). *Behavioral Ecology and Sociobiology* 56, 106–115.
6. Holy TE, and Guo Z (2005). Ultrasonic songs of male mice. *PLoS Biol.* 3, e386. [PubMed: 16248680]
7. Wohlgemuth MJ, Sober SJ, and Brainard MS (2010). Linked control of syllable sequence and phonology in birdsong. *J. Neurosci.* 30, 12936–12949. [PubMed: 20881112]
8. Moore JM, and Woolley SMN (2019). Emergent tuning for learned vocalizations in auditory cortex. *Nat. Neurosci.* 22, 1469–1476. [PubMed: 31406364]
9. Romanski LM, and Averbeck BB (2009). The primate cortical auditory system and neural representation of conspecific vocalizations. *Annu. Rev. Neurosci.* 32, 315–346. [PubMed: 19400713]
10. Roberts PD, and Portfors CV (2015). Responses to Social Vocalizations in the Dorsal Cochlear Nucleus of Mice. *Front. Syst. Neurosci.* 9, 172. [PubMed: 26733824]
11. Schöneich S, Kostarakos K, and Hedwig B (2015). An auditory feature detection circuit for sound pattern recognition. *Sci Adv* 1, e1500325. [PubMed: 26601259]
12. Clemens J, Schöneich S, Kostarakos K, Matthias Hennig R, and Hedwig B (2020). A small, computationally flexible network produces the phenotypic diversity of song recognition in crickets. *Cold Spring Harbor Laboratory*, 2020.07.27.221655.
13. Bennet-Clark HC, and Ewing AW (1967). Stimuli provided by Courtship of Male *Drosophila melanogaster*. *Nature* 215, 669–671.
14. Arthur BJ, Sunayama-Morita T, Coen P, Murthy M, and Stern DL (2013). Multi-channel acoustic recording and automated analysis of *Drosophila* courtship songs. *BMC Biol.* 11, 11. [PubMed: 23369160]
15. Coen P, Clemens J, Weinstein AJ, Pacheco DA, Deng Y, and Murthy M (2014). Dynamic sensory cues shape song structure in *Drosophila*. *Nature* 507, 233–237. [PubMed: 24598544]
16. Deutsch D, Clemens J, Thiberge SY, Guan G, and Murthy M (2019). Shared Song Detector Neurons in *Drosophila* Male and Female Brains Drive Sex-Specific Behaviors. *Curr. Biol.* 29, 3200–3215.e5. [PubMed: 31564492]
17. Clemens J, Girardin CC, Coen P, Guan X-J, Dickson BJ, and Murthy M (2015). Connecting Neural Codes with Behavior in the Auditory System of *Drosophila*. *Neuron* 87, 1332–1343. [PubMed: 26365767]
18. Albert JT, Nadrowski B, and Göpfert MC (2007). Mechanical signatures of transducer gating in the *Drosophila* ear. *Curr. Biol.* 17, 1000–1006. [PubMed: 17524645]
19. Göpfert MC, and Robert D (2002). The mechanical basis of *Drosophila* audition. *J. Exp. Biol.* 205, 1199–1208. [PubMed: 11948197]
20. Patella P, and Wilson RI (2018). Functional Maps of Mechanosensory Features in the *Drosophila* Brain. *Curr. Biol.* 28, 1189–1203.e5. [PubMed: 29657118]
21. Pacheco DA, Thiberge SY, Pnevmatikakis E, and Murthy M (2020). Auditory activity is diverse and widespread throughout the central brain of *Drosophila*. *Nat. Neurosci.* 24, 93–104. [PubMed: 33230320]
22. Tootoonian S, Coen P, Kawai R, and Murthy M (2012). Neural Representations of Courtship Song in the *Drosophila* Brain. *Journal of Neuroscience* 32, 787–798. [PubMed: 22262877]

23. Kamikouchi A, Inagaki HK, Effertz T, Hendrich O, Fiala A, Göpfert MC, and Ito K (2009). The neural basis of *Drosophila* gravity-sensing and hearing. *Nature* 458, 165–171. [PubMed: 19279630]
24. Azevedo AW, and Wilson RI (2017). Active Mechanisms of Vibration Encoding and Frequency Filtering in Central Mechanosensory Neurons. *Neuron* 96, 446–460.e9. [PubMed: 28943231]
25. Lai JS-Y, -Y. Lai JS, -J. Lo S, Dickson BJ, and -S. Chiang A (2012). Auditory circuit in the *Drosophila* brain. *Proceedings of the National Academy of Sciences* 109, 2607–2612.
26. Vaughan AG, Zhou C, Manoli DS, and Baker BS (2014). Neural pathways for the detection and discrimination of conspecific song in *D. melanogaster*. *Curr. Biol.* 24, 1039–1049. [PubMed: 24794294]
27. Yamada D, Ishimoto H, Li X, Kohashi T, Ishikawa Y, and Kamikouchi A (2018). GABAergic Local Interneurons Shape Female Fruit Fly Response to Mating Songs. *J. Neurosci.* 38, 4329–4347. [PubMed: 29691331]
28. Zhou C, Franconville R, Vaughan AG, Robinett CC, Jayaraman V, and Baker BS (2015). Central neural circuitry mediating courtship song perception in male *Drosophila*. *Elife* 4, e08477.
29. Wang K, Wang F, Forknall N, Yang T, Patrick C, Parekh R, and Dickson BJ (2020). Neural circuit mechanisms of sexual receptivity in *Drosophila* females. *Nature* 589, 577–581. [PubMed: 33239786]
30. Wang F, Wang K, Forknall N, Parekh R, and Dickson BJ (2020). Circuit and Behavioral Mechanisms of Sexual Rejection by *Drosophila* Females. *Current Biology* 30, 3749–3760.e3. [PubMed: 32795445]
31. Dorkenwald S, McKellar CE, Macrina T, Kemnitz N, Lee K, Lu R, Wu J, Popovych S, Mitchell E, Nehoran B, et al. (2022). FlyWire: online community for whole-brain connectomics. *Nat. Methods* 19, 119–128. [PubMed: 34949809]
32. Matsuo E, Seki H, Asai T, Morimoto T, Miyakawa H, Ito K, and Kamikouchi A (2016). Organization of projection neurons and local neurons of the primary auditory center in the fruit fly *Drosophila melanogaster*. *J. Comp. Neurol.* 524, 1099–1164. [PubMed: 26762251]
33. Scheffer LK, Xu CS, Januszewski M, Lu Z, Takemura S-Y, Hayworth KJ, Huang GB, Shinomiya K, Maitlin-Shepard J, Berg S, et al. (2020). A connectome and analysis of the adult central brain. *eLife* 9, e57443. [PubMed: 32880371]
34. Chen T-W, Wardill TJ, Sun Y, Pulver SR, Renninger SL, Baohan A, Schreiter ER, Kerr RA, Orger MB, Jayaraman V, et al. (2013). Ultrasensitive fluorescent proteins for imaging neuronal activity. *Nature* 499, 295–300. [PubMed: 23868258]
35. Morley EL, Jonsson T, and Robert D (2018). Auditory sensitivity, spatial dynamics, and amplitude of courtship song in *Drosophila melanogaster*. *J. Acoust. Soc. Am.* 144, 734. [PubMed: 30180716]
36. Dolan M-J, Frechter S, Bates AS, Dan C, Huoviala P, Roberts RJV, Schlegel P, Dhawan S, Tabano R, Dionne H, et al. (2019). Neurogenetic dissection of the *Drosophila* lateral horn reveals major outputs, diverse behavioural functions, and interactions with the mushroom body. *eLife* 8, e43079. [PubMed: 31112130]
37. Suver MP, Matheson AMM, Sarkar S, Damiata M, Schoppik D, and Nagel KI (2019). Encoding of wind direction by central neurons in *Drosophila*. *Neuron* 102, 828–842.E7. [PubMed: 30948249]
38. Coates KE, Calle-Schuler SA, Helmick LM, Knotts VL, Martik BN, Salman F, Warner LT, Valla SV, Bock DD, and Dacks AM (2020). The wiring logic of an identified serotonergic neuron that spans sensory networks. *Journal of Neuroscience* 40, 6309–6327. [PubMed: 32641403]
39. Zheng Z, Lauritzen JS, Perlman E, Robinson CG, Nichols M, Milkie D, Torrens O, Price J, Fisher CB, Sharifi N, et al. (2018). A Complete Electron Microscopy Volume of the Brain of Adult *Drosophila melanogaster*. *Cell* 174, 730–743.e22. [PubMed: 30033368]
40. Clemens J, Coen P, Roemschied FA, Pereira TD, Mazumder D, Aldarondo DE, Pacheco DA, and Murthy M (2018). Discovery of a New Song Mode in *Drosophila* Reveals Hidden Structure in the Sensory and Neural Drivers of Behavior. *Curr. Biol.* 28, 2400–2412.e6. [PubMed: 30057309]
41. Buhmann J, Sheridan A, Gerhard S, Krause R, Nguyen T, Heinrich L, Schlegel P, Lee W-CA, Wilson R, Saalfeld S, et al. (2019). Automatic Detection of Synaptic Partners in a Whole-Brain *Drosophila* EM Dataset. *bioRxiv*, 10.1101/2019.12.12.874172.

42. Eckstein N, Bates AS, Du M, Hartenstein V, Gregory SX, and Funke J (2020). Neurotransmitter Classification from Electron Microscopy Images at Synaptic Sites in *Drosophila*. *bioRxiv*, 10.1101/2020.06.12.148775.
43. Buhmann J, Sheridan A, Malin-Mayor C, Schlegel P, Gerhard S, Kazimiers T, Krause R, Nguyen TM, Heinrich L, Lee W-CA, et al. (2021). Automatic detection of synaptic partners in a whole-brain *Drosophila* electron microscopy data set. *Nature Methods* 18, 771–774. [PubMed: 34168373]
44. McInnes L, Healy J, and Melville J (2018). UMAP: Uniform Manifold Approximation and Projection for Dimension Reduction. *arXiv [stat.ML]*.
45. Mezzera C, Brotas M, Gaspar M, Pavlou HJ, Goodwin SF, and Vasconcelos ML (2020). Ovipositor Extrusion Promotes the Transition from Courtship to Copulation and Signals Female Acceptance in *Drosophila melanogaster*. *Curr. Biol.* 30, 3736–3748.e5. [PubMed: 32795437]
46. Kim H, Horigome M, Ishikawa Y, Li F, Lauritzen JS, Card G, Bock DD, and Kamikouchi A (2020). Wiring patterns from auditory sensory neurons to the escape and song-relay pathways in fruit flies. *J. Comp. Neurol.* 528, 2068–2098. [PubMed: 32012264]
47. Corominas-Murtra B, Goñi J, Solé RV, and Rodríguez-Caso C (2013). On the origins of hierarchy in complex networks. *Proc. Natl. Acad. Sci. U. S. A.* 110, 13316–13321. [PubMed: 23898177]
48. Oja E (1992). Principal components, minor components, and linear neural networks. *Neural Netw.* 5, 927–935.
49. Ganguli S, Huh D, and Sompolinsky H (2008). Memory traces in dynamical systems. *Proc. Natl. Acad. Sci. U. S. A.* 105, 18970–18975. [PubMed: 19020074]
50. Liu TX, Davoudian PA, Lizbinski KM, and Jeanne JM (2022). Connectomic features underlying diverse synaptic connection strengths and subcellular computation. *Curr. Biol.* 32, 559–569.e5. [PubMed: 34914905]
51. Sproule MKJ, and Chacron MJ (2017). Electrosensory neural responses to natural electro-communication stimuli are distributed along a continuum. *PLoS One* 12, e0175322. [PubMed: 28384244]
52. Thompson AW, and Scott EK (2016). Characterisation of sensitivity and orientation tuning for visually responsive ensembles in the zebrafish tectum. *Sci. Rep.* 6, 34887. [PubMed: 27713561]
53. Minderer M, Brown KD, and Harvey CD (2019). The Spatial Structure of Neural Encoding in Mouse Posterior Cortex during Navigation. *Neuron* 102, 232–248.e11. [PubMed: 30772081]
54. Raposo D, Kaufman MT, and Churchland AK (2014). A category-free neural population supports evolving demands during decision-making. *Nat. Neurosci.* 17, 1784–1792. [PubMed: 25383902]
55. Saleem AB, Ayaz A, Jeffery KJ, Harris KD, and Carandini M (2013). Integration of visual motion and locomotion in mouse visual cortex. *Nat. Neurosci.* 16, 1864–1869. [PubMed: 24185423]
56. Namiki S, Dickinson MH, Wong AM, Korff W, and Card GM (2018). The functional organization of descending sensory-motor pathways in. *Elife* 7.
57. Rayshubskiy A, Holtz SL, D’Alessandro I, Li AA, Vanderbeck QX, Haber IS, Gibb PW, and Wilson RI (2020). Neural circuit mechanisms for steering control in walking *Drosophila*. *bioRxiv*, 10.1101/2020.04.04.024703.
58. Batchelor AV, and Wilson RI (2019). Sound localization behavior in depends on inter-antenna vibration amplitude comparisons. *J. Exp. Biol.* 222.
59. Fuchs PA, and Lauer AM (2019). Efferent Inhibition of the Cochlea. *Cold Spring Harb. Perspect. Med.* 9.
60. Winer JA, and Schreiner CE (2005). The Central Auditory System: A Functional Analysis. In *The Inferior Colliculus*, Winer JA and Schreiner CE, eds. (Springer), pp. 1–68.
61. Stumpner A (2002). A species-specific frequency filter through specific inhibition, not specific excitation. *Journal of Comparative Physiology A: Sensory, Neural, and Behavioral Physiology* 188, 239–248.
62. Romer H, Rheinlaender J, and Dronse R (1981). Intracellular studies on auditory processing in the metathoracic ganglion of the locust. *Journal of Comparative Physiology A* 144, 305–312.
63. Woolley SMN, and Portfors CV (2013). Conserved mechanisms of vocalization coding in mammalian and songbird auditory midbrain. *Hear. Res.* 305, 45–56. [PubMed: 23726970]

64. Wyttenbach RA, May ML, and Hoy RR (1996). Categorical perception of sound frequency by crickets. *Science* 273, 1542–1544. [PubMed: 8703214]
65. Rose GJ, and Brenowitz EA (2002). Pacific treefrogs use temporal integration to differentiate advertisement from encounter calls. *Animal Behaviour* 63, 1183–1190.
66. Cohen Y, Shen J, Semu D, Leman DP, Liberti WA 3rd, Perkins LN, Liberti DC, Kotton DN, and Gardner TJ (2020). Hidden neural states underlie canary song syntax. *Nature* 582, 539–544. [PubMed: 32555461]
67. Calhoun AJ, Pillow JW, and Murthy M (2019). Unsupervised identification of the internal states that shape natural behavior. *Nat. Neurosci.* 22, 2040–2049. [PubMed: 31768056]
68. Luan H, Peabody NC, Vinson CR, and White BH (2006). Refined spatial manipulation of neuronal function by combinatorial restriction of transgene expression. *Neuron* 52, 425–436. [PubMed: 17088209]
69. Pfeiffer BD, Ngo T-TB, Hibbard KL, Murphy C, Jenett A, Truman JW, and Rubin GM (2010). Refinement of tools for targeted gene expression in *Drosophila*. *Genetics* 186, 735–755. [PubMed: 20697123]
70. Tirian L, and Dickson BJ (2017). The VT GAL4, LexA, and split-GAL4 driver line collections for targeted expression in the *Drosophila* nervous system. *bioRxiv*, 10.1101/198648.
71. Dionne H, Hibbard KL, Cavallaro A, Kao J-C, and Rubin GM (2018). Genetic Reagents for Making Split-GAL4 Lines in. *Genetics* 209, 31–35. [PubMed: 29535151]
72. Jenett A, Rubin GM, Ngo T-TB, Shepherd D, Murphy C, Dionne H, Pfeiffer BD, Cavallaro A, Hall D, Jeter J, et al. (2012). A GAL4-driver line resource for *Drosophila* neurobiology. *Cell Rep.* 2, 991–1001. [PubMed: 23063364]
73. Otsuna H, Ito M, and Kawase T (2018). Color depth MIP mask search: a new tool to expedite Split-GAL4 creation. *bioRxiv*, 10.1101/318006.
74. Nern A, Pfeiffer BD, and Rubin GM (2015). Optimized tools for multicolor stochastic labeling reveal diverse stereotyped cell arrangements in the fly visual system. *Proceedings of the National Academy of Sciences* 112, E2967–E2976.
75. Wu M, Nern A, Ryan Williamson W, Morimoto MM, Reiser MB, Card GM, and Rubin GM (2016). Visual projection neurons in the *Drosophila* lobula link feature detection to distinct behavioral programs. *eLife* 5, e21022. [PubMed: 28029094]
76. Aso Y, Hattori D, Yu Y, Johnston RM, Iyer NA, Ngo T-TB, Dionne H, Abbott LF, Axel R, Tanimoto H, et al. (2014). The neuronal architecture of the mushroom body provides a logic for associative learning. *Elife* 3, e04577. [PubMed: 25535793]
77. Wan Y, Otsuna H, Chien C-B, and Hansen C (2009). An interactive visualization tool for multi-channel confocal microscopy data in neurobiology research. *IEEE Trans. Vis. Comput. Graph.* 15, 1489–1496. [PubMed: 19834225]
78. Wan Y, Otsuna H, Chien C-B, and Hansen C (2012). FluoRender: An Application of 2D Image Space Methods for 3D and 4D Confocal Microscopy Data Visualization in Neurobiology Research. *IEEE Pac. Vis. Symp*, 201–208. [PubMed: 23584131]
79. Rohlfing T (2011). User guide to the computational morphometry toolkit. Neuroscience Program, SRI International, Menlo Park, CA 3.
80. Ito K, Shinomiya K, Ito M, Armstrong JD, Boyan G, Hartenstein V, Harzsch S, Heisenberg M, Homberg U, Jenett A, et al. (2014). A systematic nomenclature for the insect brain. *Neuron* 81, 755–765. [PubMed: 24559671]
81. Bates AS, Manton JD, Jagannathan SR, Costa M, Schlegel P, Rohlfing T, and Jefferis GS (2020). The natverse, a versatile toolbox for combining and analysing neuroanatomical data. *Elife* 9, e53350. [PubMed: 32286229]
82. Bogovic JA, Otsuna H, Heinrich L, Ito M, Jeter J, Meissner G, Nern A, Colonell J, Malkesman O, Ito K, et al. (2020). An unbiased template of the *Drosophila* brain and ventral nerve cord. *PLoS One* 15, e0236495. [PubMed: 33382698]
83. Xu CS, Januszewski M, Lu Z, Takemura S-Y, Hayworth KJ, Huang G, Shinomiya K, Maitin-Shepard J, Ackerman D, Berg S, et al. (2020). A Connectome of the Adult *Drosophila* Central Brain. *bioRxiv*, 10.1101/2020.01.21.911859.

84. Deutsch D, Pacheco DA, Encarnacion-Rivera LJ, Pereira T, Fathy R, Calhoun A, Ireland EC, Burke AT, Dorkenwald S, McKellar C, et al. (2020). The Neural Basis for a Persistent Internal State in *Drosophila* Females. *bioRxiv*, 10.1101/2020.02.13.947952.
85. Murthy M, and Turner G (2013). Dissection of the head cuticle and sheath of living flies for whole-cell patch-clamp recordings in the brain. *Cold Spring Harb. Protoc.* 2013, 134–139. [PubMed: 23378645]
86. Clemens J, Ozeri-Engelhard N, and Murthy M (2018). Fast intensity adaptation enhances the encoding of sound in *Drosophila*. *Nat. Commun.* 9, 134. [PubMed: 29317624]
87. Göpfert MC, Albert JT, Nadrowski B, and Kamikouchi A (2006). Specification of auditory sensitivity by *Drosophila* TRP channels. *Nat. Neurosci.* 9, 999–1000. [PubMed: 16819519]
88. Park M, and Pillow JW (2011). Receptive field inference with localized priors. *PLoS Comput. Biol.* 7, e1002219. [PubMed: 22046110]
89. Baker CA, and Carlson BA (2014). Short-term depression, temporal summation, and onset inhibition shape interval tuning in midbrain neurons. *J. Neurosci.* 34, 14272–14287. [PubMed: 25339741]
90. Groh JM, Kelly KA, and Underhill AM (2003). A monotonic code for sound azimuth in primate inferior colliculus. *J. Cogn. Neurosci.* 15, 1217–1231. [PubMed: 14709238]
91. Klapoetky NC, Murata Y, Kim SS, Pulver SR, Birdsey-Benson A, Cho YK, Morimoto TK, Chuong AS, Carpenter EJ, Tian Z, et al. (2014). Independent optical excitation of distinct neural populations. *Nature Meth.* 11, 338–346.

Highlights

- *D. melanogaster* auditory neurons exhibit a continuum of courtship song preferences
- The auditory connectome is densely interconnected without hierarchical organization
- Auditory responses can be predicted from the wiring diagram

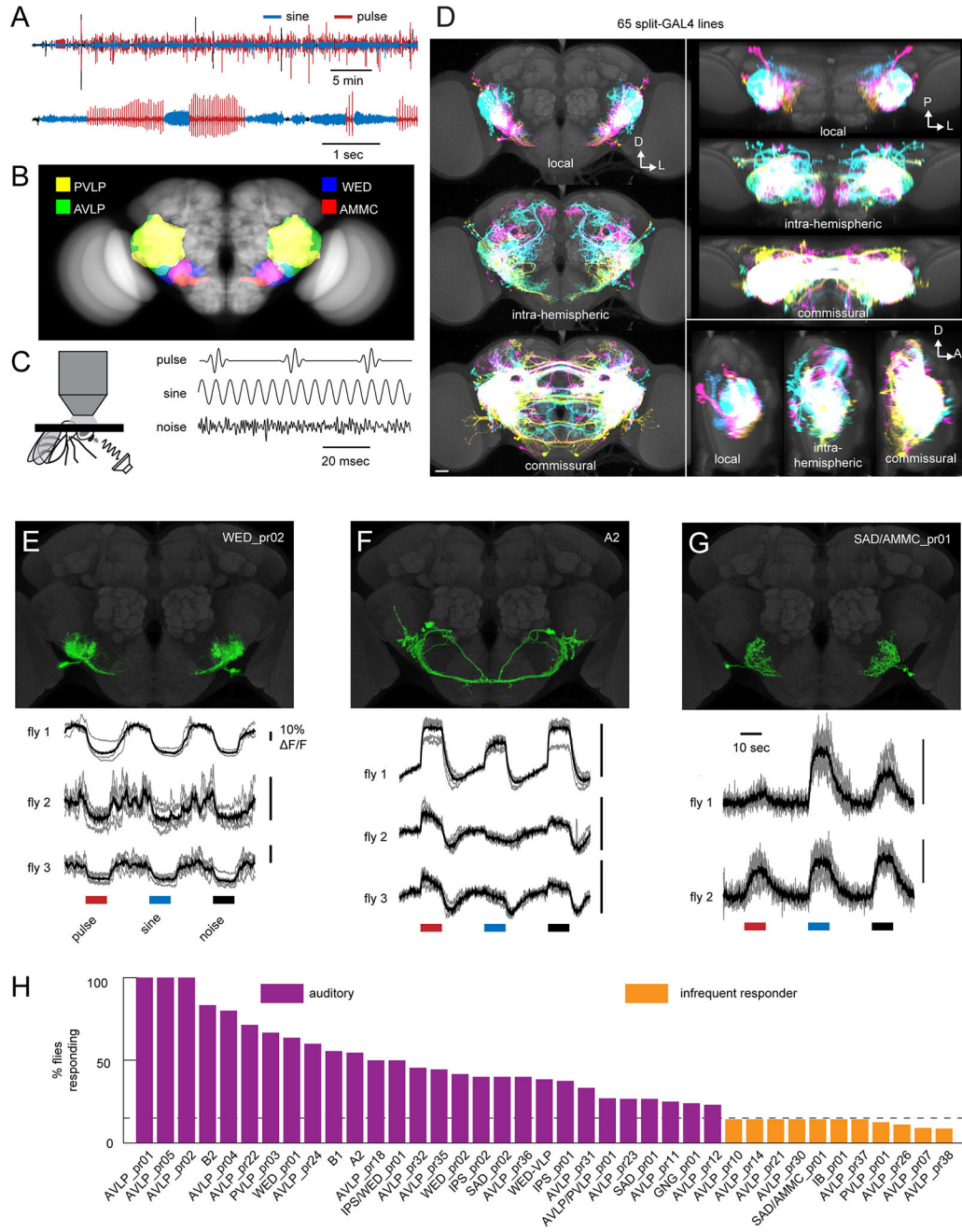


Figure 1. Anatomic and functional screen for auditory neurons.

A) Microphone recording from a single wild-type (CS-Tully strain) male fly paired with a virgin female. The top trace shows song over 30 minutes, and the bottom trace shows a close-up of song bouts consisting of switches between the pulse and sine song modes. B) Primary auditory neurons called Johnston Organ neurons in the antenna project to the antennal mechanosensory and motor center (AMMC) in the central brain. Auditory information is then routed to downstream areas including the wedge (WED), anterior ventrolateral protocerebrum (AVLP), and posterior ventrolateral protocerebrum (PVLVP). See Table S1 for neuropil abbreviations. C) Schematic showing two-photon calcium imaging

set-up with sound delivered to the arista (left) and calibrated, synthetic acoustic stimuli used to search for auditory responses (right). 100 msec of each stimulus is shown.

D) Overlaid images of the split-GAL4 collection's local interneurons, intra-hemispheric projection neurons, or commissural neurons, segmented from aligned images of the split GAL4 collection (see also Data S1A–B) and shown as maximum projections from the front (left), top (top right), and side (bottom right). Each cell type was colored randomly. D: dorsal; L: lateral; P: posterior; A: anterior. Scale bar: 25 microns. E–G) Calcium responses to pulse, sine, and noise stimuli from three cell classes (see also Figure S1D–E). In the calcium traces, each trial is shown in grey and the mean across trials is shown in black. H) Percentage of imaged flies from each cell class with auditory responses. We defined auditory cell classes as those in which >15% (dotted line) of imaged flies responded to the pulse, sine, or noise stimuli. If at least 1 fly but fewer than 15% of imaged flies responded, we termed the cell class an 'infrequent responder'. If no flies responded (out of 4–6 total flies), we termed the cell class 'non-auditory'. Numbers of flies imaged ranged from 4–17 for auditory cell classes, and from 7–23 for infrequently responding cell classes. See Table S2 and Data S1C for cell class images and names. See also Tables S1–2.

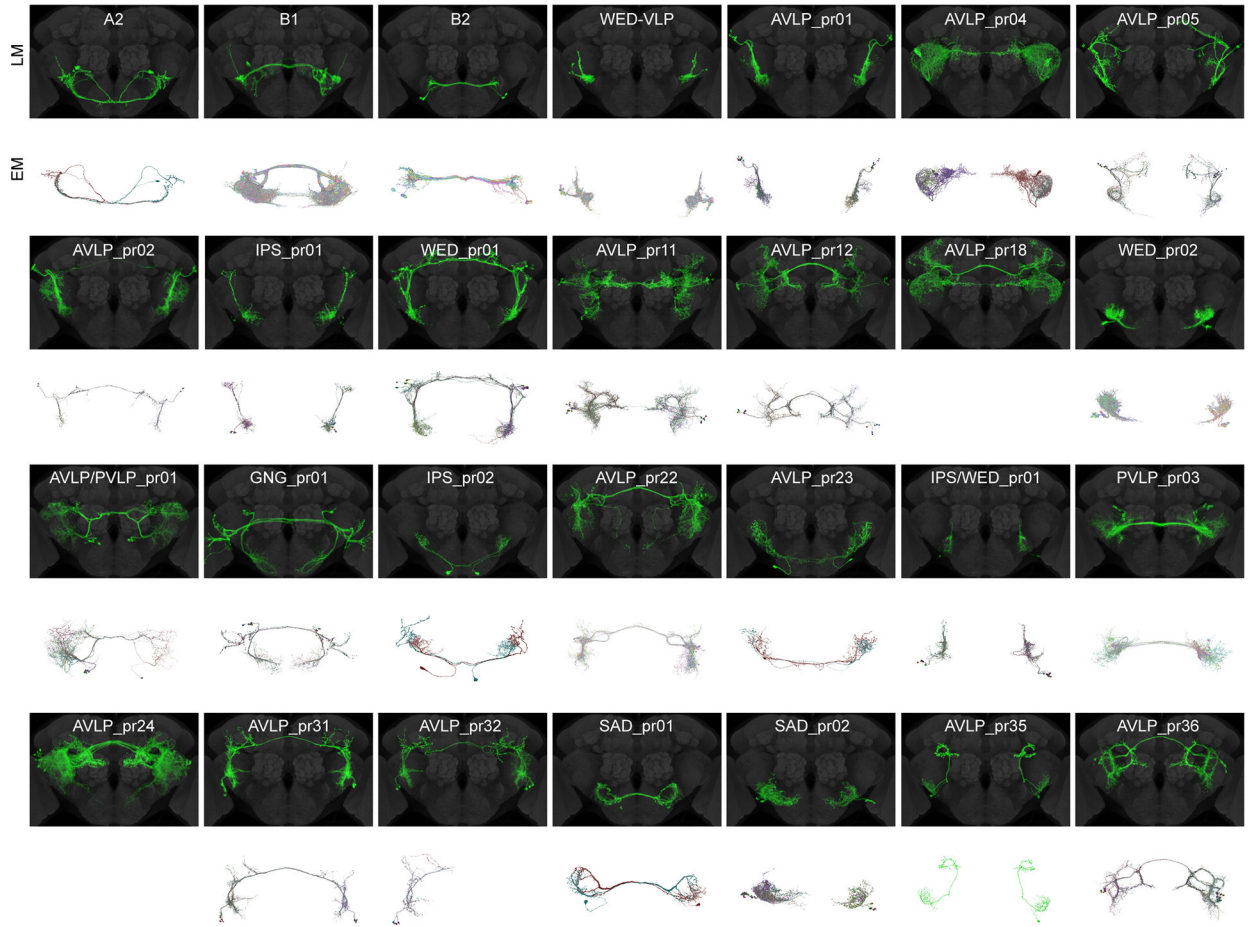


Figure 2. Light microscopic (LM) and electron microscopic (EM) images of auditory WED/VLP cell types.

Aligned central brains with expression patterns of WED/VLP neuron classes digitally segmented (see Data S1B–C). Only those cell classes with auditory responses are shown. Gray: nc82. Below each brain expression pattern are the EM reconstructions (identified and proofread in FlyWire.ai, see Table S3) corresponding to each cell class. There was insufficient information in the split-GAL4 and stochastic labeling expression patterns to resolve the EM reconstructions representing two cell classes (AVLP_pr18 and AVLP_pr24). EM reconstructions representing cell type AVLP_pr32 were only found in one hemisphere. AVLP_pr01 and AVLP_pr02 share morphological similarities with vpoINs, which provide sound-evoked inhibition onto descending neurons called vpoDNs that contribute to vaginal plate opening (Wang et al., 2020b). Based on both FlyWire and hemibrain connections, vpoINs (defined as inputs to vpoDN with morphology consistent with vpoINs) consist of two subtypes: one with a commissure, and one with a medial projection that does not cross the midline. This leads us to conclude that AVLP_pr02 are likely the commissural vpoINs, but AVLP_pr01 are a cell type independent from vpoINs. See also Figures S2 and S3 and Tables S2 and S3.

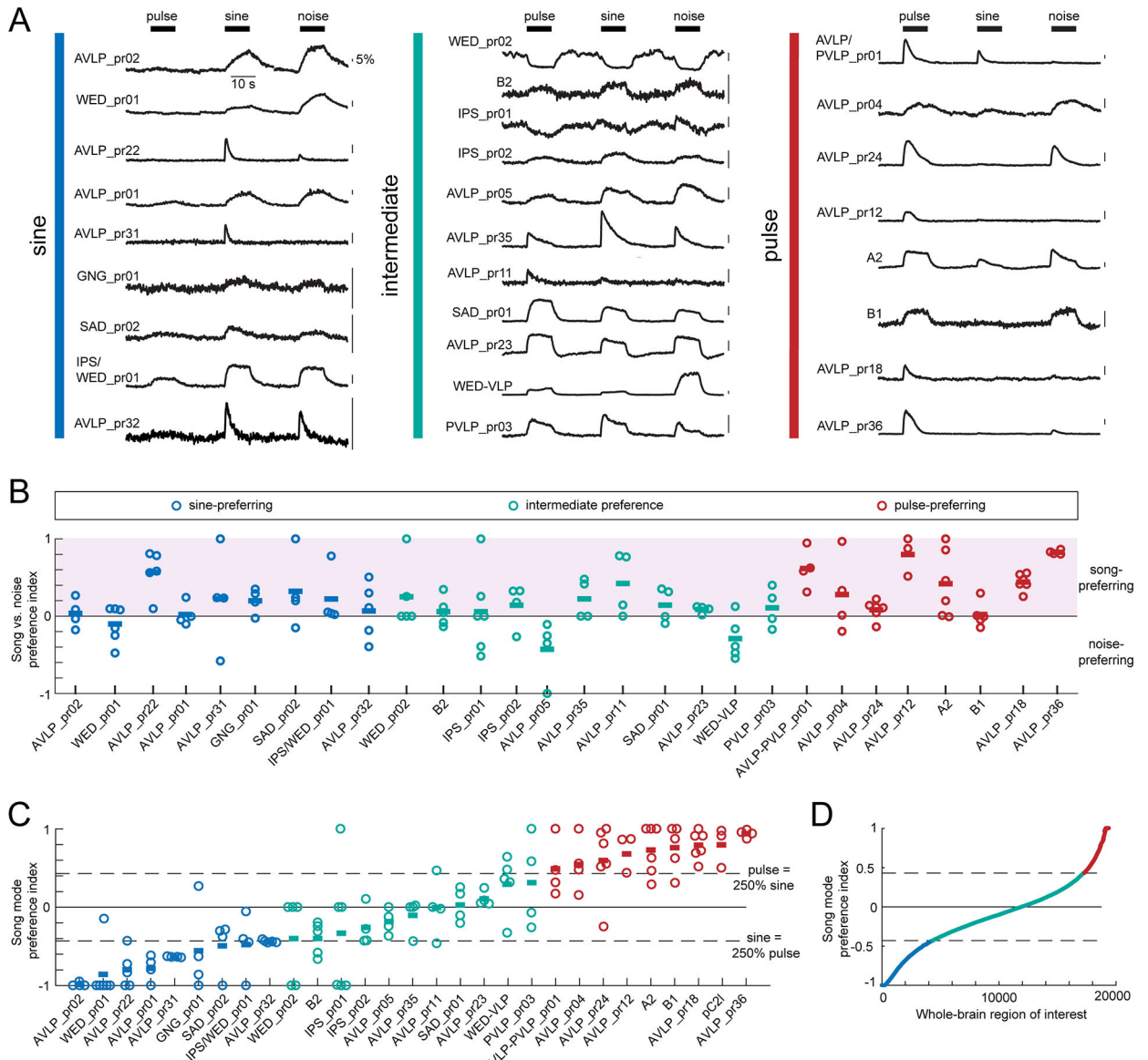


Figure 3. Auditory WED/VLP neurons show a continuum of preferences for sine and pulse song modes.

A) Trial-averaged representative calcium traces for a single fly from each cell class in response to pulse, sine, and noise stimuli. Vertical colored bars indicate the pulse- vs. sine-preference of each cell class given in (C). B) The integrals of responses to pulse, sine, and noise were used to calculate a song vs. noise preference index, which ranges from -1 (strongest noise preference) to 1 (strongest song preference) (see Methods and Figure S1A–B). The color of the dots reflect the pulse- vs. sine-preference of each cell class given in (C). Each dot represents the responses of one fly, and horizontal lines represent the mean within each cell type. To identify sine-preferring cell types, we required the mean preference index across flies to be below -0.43 , which corresponds to a sine response that is at least 250% that of pulse. To identify pulse-preferring cell types, we required the mean preference index across flies to be above -0.43 , which corresponds to a pulse response that is at least

250% that of sine. All other cell types were classified as having intermediate song mode preference. The song mode preference index for pC2l was calculated using data from a previous study¹⁶. Each dot represents the responses of one fly, and horizontal lines represent the mean within each cell type. There was no correlation between song vs. noise preference in (B) and song mode preference in (C) (Spearman's $\rho=0.15$, $p=0.071$, $n=143$ flies). Tan dots indicate cell types that contact JONs (see Figure S4B). See also Figure S1D–F for response variability and Figure S2 for the neuropils innervated by neurons from each song mode preference class. D) The song mode preference index for 19,389 auditory-responsive regions of interest (ROIs) from the entire central brain, obtained via pan-neuronal imaging in a previous study²¹. See also Figures S1–3 and Table S2.

Author Manuscript

Author Manuscript

Author Manuscript

Author Manuscript

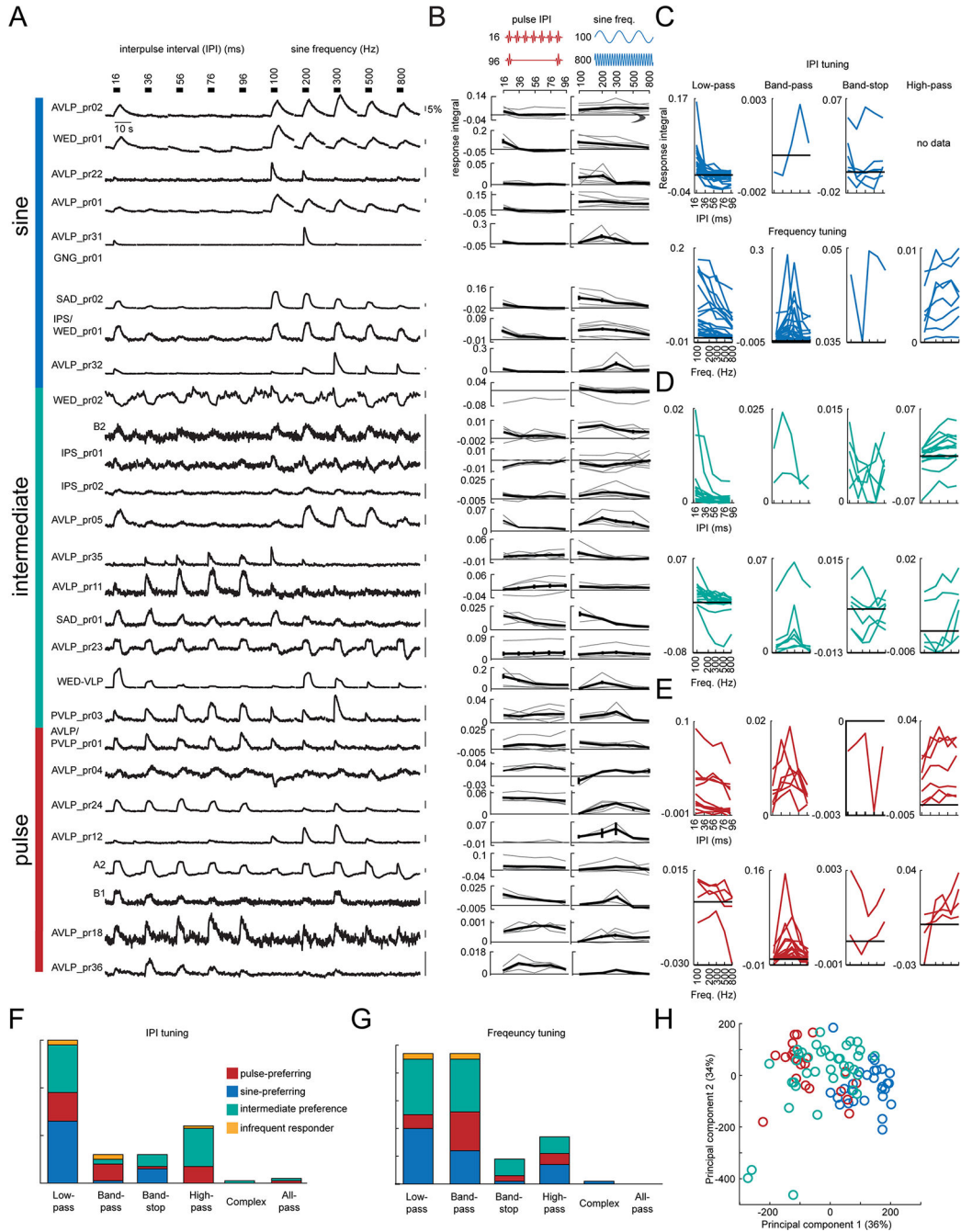


Figure 4. Pulse rate (interpulse interval) and frequency tuning.

A) Trial-averaged representative calcium traces in response to pulse rate (interpulse interval (IPI)) and sine frequency stimuli. B) Pulse rate (left) and sine frequency (right) tuning curves. The tuning curves from individual flies are shown in grey, and the average across flies is shown in black. Error bars report standard error. C-E) Tuning curves for each fly recorded in the data set. Tuning curves are colored according to the song mode preference of each WED/VLP neuron type. F-G) Histogram of IPI (F) and frequency (G) tuning types across the dataset. Responses that were roughly equal for every stimulus were classified as all-pass, and responses that did not fit any other category were classified as complex (see

Methods). H) Principal components analysis (PCA) on the response integrals elicited by IPI and frequency stimuli. Each dot represents one recording, and the color represents the song mode preference for each cell type. PC1 positively correlates with responses to 100 and 200 Hz stimuli, and negatively correlates with responses to 36–96 ms IPI stimuli. PC2 positively correlates with responses to 16 and 36 ms stimuli, and negatively correlates with responses to 100 and 800 Hz stimuli. See also Table S2.

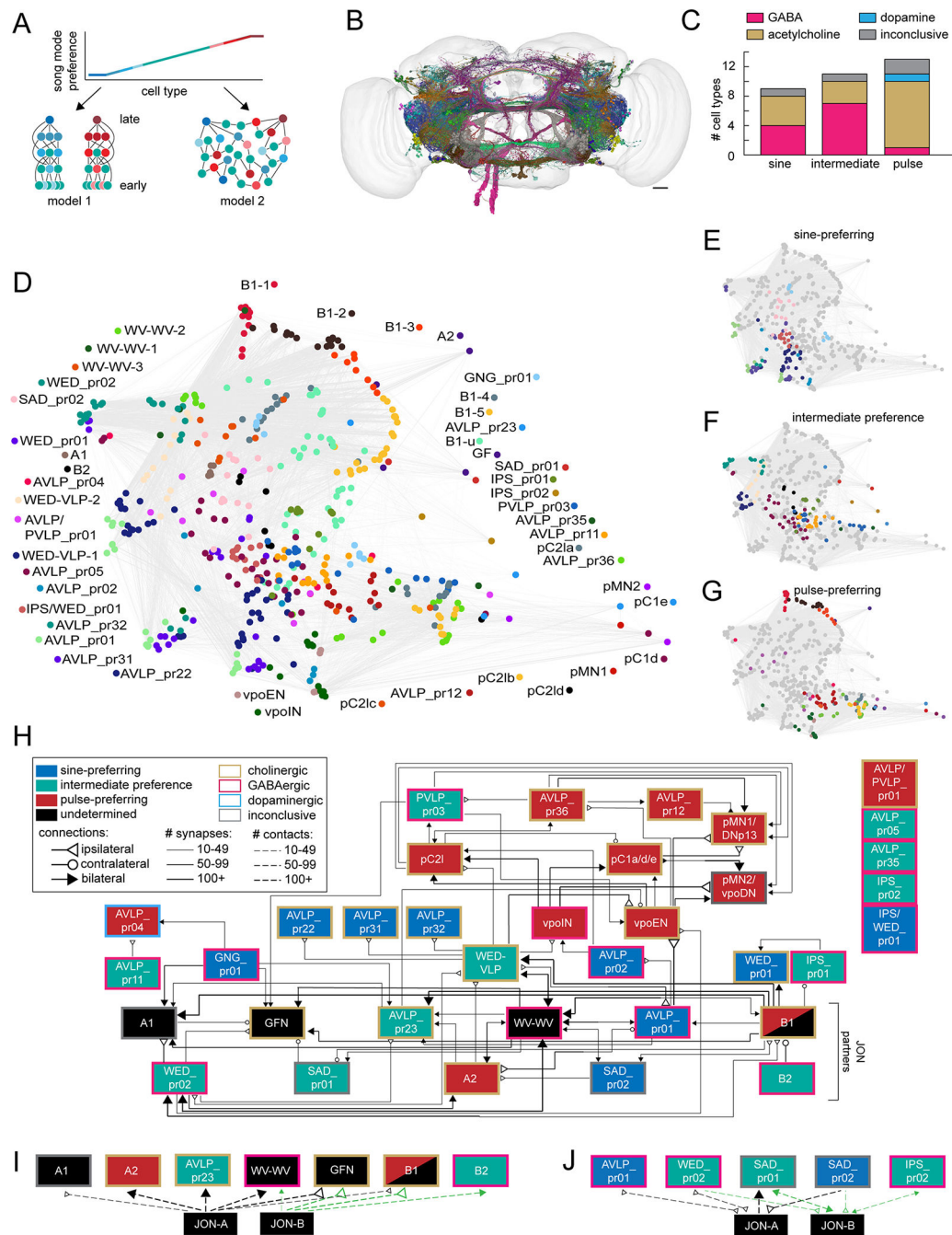


Figure 5. The auditory connectome.

A) Two models for the organization of auditory pathways underlying the observed continuum of song mode preferences. Each circle represents a cell type, and each line represents synaptic connections. Red = pulse-preferring, blue = sine-preferring, and green = intermediate preference (see Figure 3C). The shading of red and blue neurons indicates the strength of pulse or sine preference, respectively. In model 1, neurons selective for pulse and sine are separated into distinct pathways, with neurons of intermediate preferences playing roles in both pathways (left). Within-mode connections sharpen tuning for song features. See

Figure S3 for evidence of anatomic separation between pulse and sine pathways, supporting model 1. In model 2, neurons of different song mode preferences are highly interconnected at all levels without hierarchical organization (right). Downstream neurons may pool the responses of diversely tuned neurons to establish selectivity for a variety of song parameters. B) To test these models, we examined synaptic connections among auditory neurons (N=479 neurons from 48 cell types) in an electron microscopic volume of an entire female fly brain (see Figure S4A). D) Representation of the synaptic connectivity of auditory neurons using uniform manifold approximation and projection (UMAP). Each dot represents one neuron, the color of the dot represents the cell type, and lines represent synaptic connections. E-G) Same as D but for only sine-preferring (E), intermediate preference (F), or pulse-preferring (G) neurons. H) Flow-chart diagram of the auditory connectome. Each box represents a cell type, and each line represents a synaptic connection (see Methods for connection criteria). The song mode preference of A2, B2, and WED-VLP come from recordings from the split-GAL4 lines labeling those neurons (Figure 3C; Table S2), and the song preferences of several higher-order and descending neurons (pC21a-c, vpoEN, vpoIN, pC1a,d,e, pMN1/DNp13, and pMN2/vpoDN) come from previous studies^{16,28–30}. Cell types shown in black boxes have not had their sine/pulse preference determined. B1 shading reflects the observation that the split-GAL4 line we imaged from, while pulse-preferring, labels only a handful of B1 cells, and the tuning of the remaining B1 cells remains to be determined (but see²⁴. Five cell types formed no connections with other neurons in the dataset. See Figure S5 for neurotransmitter determination and connections of auditory cells with previously reported subtypes (ie, WED-VLP, WV-WV, and B1). See Methods for how the connectivity diagram was formed from identified reconstructions in FlyWire.ai. I) Diagram of connections between JONs and auditory cell types in which JONs are presynaptic (as measured by number of membrane contacts; see Methods and Figure S4B–E). Connections with JON-As are shown in black, and connections with JON-Bs are shown in orange. J) Same as (I) for connections in which auditory cell types are presynaptic to JONs. See also Figures S4–5 and Tables S2–3.

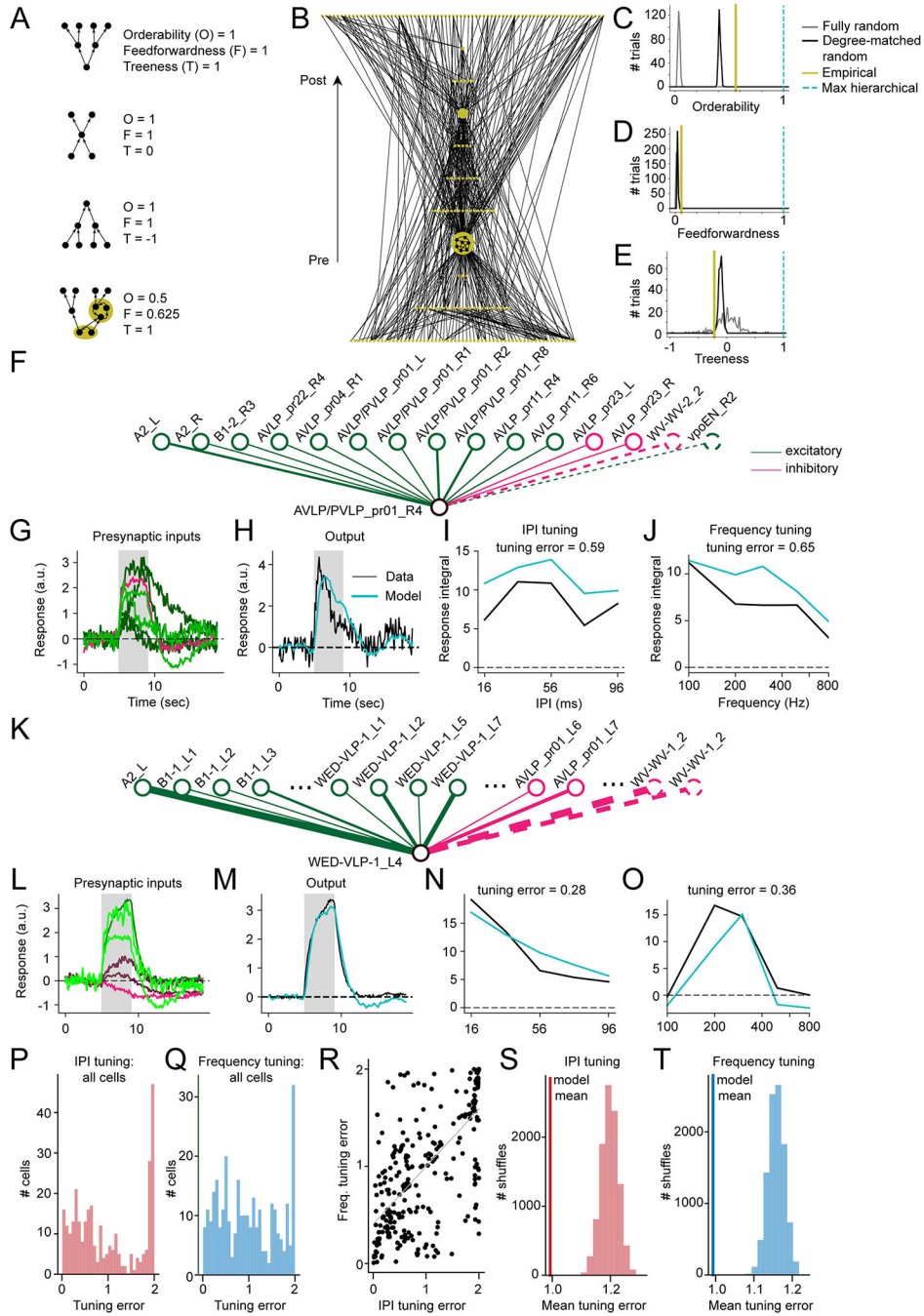


Figure 6. Evaluating the hierarchical structure of the auditory network and emergence of postsynaptic tuning curves from connectome-weighted presynaptic responses.
A) Measures of hierarchical structure (orderability, feedforwardness, and treeness) for four simple networks (reproduced from ⁴⁷); each gold region highlights a strongly connected component (a set of neurons all mutually reachable from one another via at least one directed path). B) Hierarchically displayed node-weighted graph condensation of the empirically measured auditory network. Each node in the condensation is a strongly connected component of the original auditory network, with node size indicating the number of neurons in the component (minimum 1 neuron, maximum 124 neurons). Connections

are oriented upward with postsynaptic targets displayed above presynaptic sources. C) Orderability of the auditory network, computed from the original network and the graph condensation (A), as compared to 300 instantiations (trials) of either a fully random network (with only neuron count and connection probability matched to the original auditory network) or degree-matched random network (in which each neuron's incoming and outgoing connection numbers were inherited from the empirical network but connections were otherwise randomized). D) Feedforwardness of the auditory network, as compared to fully random and degree-matched random networks. The low value arises from most paths passing through the largest connected component. E) Treeness of the auditory network, as compared to fully random and degree-matched random networks. Prior to analysis, connections between two neurons in the original network were only counted if at least 10 synapses were detected (171 out of 476 neurons were unconnected to the main network and left out of the calculations). A maximally hierarchical network has a feedforwardness, orderability, and treeness of 1 (cyan; C-E). F) Schematic of network model used to compute neural responses and tuning for cell AVLP/PVLP_pr01_R4 (lower node). Upper nodes represent input neurons and lines indicate synaptic connections. Solid lines represent inputs from imaged split-GAL4 lines and dotted lines represent inputs from neurons outside our imaging dataset. G) Normalized responses of cells presynaptic to AVLP/PVLP_pr01_R4 (15 total, 2 without tuning data), in response to 36 ms IPI stimulus. Coloring shows weight of presynaptic cell onto postsynaptic cell, with brighter green or red indicating stronger excitatory and inhibitory weights, respectively. The grey box indicates when the stimulus was on. H) Observed postsynaptic response to the same 36 ms IPI stimulus (black) vs response modeled by feeding presynaptic responses through the network model (teal). I) IPI tuning curves from observed and modeled postsynaptic responses, computed by integrating responses from stimulus onset to 4 seconds post stimulus offset. J) Same as (I) for sine frequency tuning. K-O) Same as (F-J) for cell WED-VLP-1_L4 (29 total, 3 without tuning data). Ellipses in (K) indicate additional neurons in the data that we did not have room to show in the diagram. P) Root mean squared error between true and modeled IPI tuning curves across all cells with both post- and presynaptic tuning data ($N = 306$ cells); tuning curves were z-scored first to compare shape rather than magnitude. Q) Same as (P) for sine frequency tuning curves. R) IPI tuning error vs. sine frequency tuning error across cells ($N=306$ cells, $R = 0.671$, $p < 10^{-39}$; Wald test with zero-slope null hypothesis). S) Histogram of mean errors computed by shuffling true relative to modeled tuning curves across cells (10000 shuffles, $p < 0.0001$, computed by counting number of shuffles yielding a mean value less than the observed mean). Vertical line indicates the mean from (P). T) Same as (S) for frequency tuning curves ($p < 0.0001$). Vertical line indicates the mean from (Q). See also Table S2.

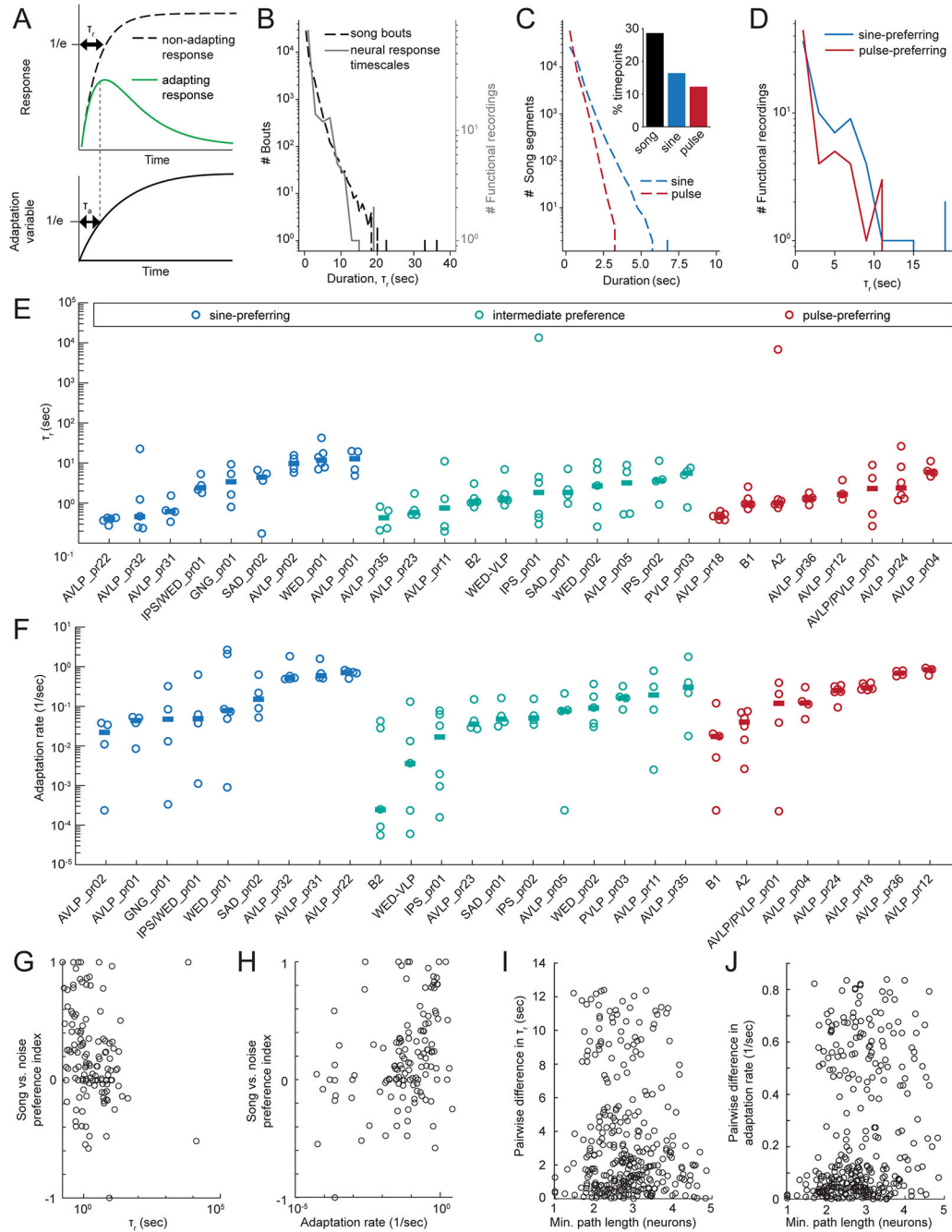


Figure 7. Response time courses are matched to song statistics.

A) Schematic of calculation of response time constant τ_r and adaptation time constant τ_a (see Methods). The neuron's total response is modeled by the green curve. B) Distribution of song bout durations (dotted line) and best fit response timescales τ_r to imaged neurons (grey). Song data was recorded during a naturalistic courtship assay in a previous experiment¹⁵; data available from⁶⁷). Song was recorded with a microphone then downsampled to 30 Hz; each downsampled frame was labeled either sine, pulse, or quiet. Bouts were defined as contiguous singing periods (quiet periods of only 1 frame were ignored in separating bouts). C) Distribution of contiguous pulse and sine song segment

Key resources table

REAGENT or RESOURCE	SOURCE	IDENTIFIER
Antibodies		
rabbit anti-GFP	Invitrogen	#A11122
mouse anti-Bruchpilot	Developmental Studies Hybridoma Bank	mAb nc82
Alexa Fluor 488-goat anti-rabbit	ThermoFisher	A11034
Alexa Fluor 568-goat anti-mouse	ThermoFisher	A11031
Rat anti-FLAG Tag	Novus Biologicals	NBP1-06712
Rabbit anti-HA tag	Cell Signal Technologies	3724S
Cy2 goat anti-mouse	Jackson Immuno Research	115-225-166
ATTO647N goat anti-rat IgG	Rockland	612-156-120
AF594 donkey anti-rabbit	Jackson Immuno Research	711-585-152
DL550 mouse anti-V5 Tag	AbD Serotec	MCA1360D550GA
Bacterial and virus strains		
Biological samples		
Chemicals, peptides, and recombinant proteins		
Critical commercial assays		
Deposited data		
Experimental models: Cell lines		
Experimental models: Organisms/strains		
<i>D. melanogaster</i> : 20xUAS-GCaMP6s, td-Tomato/Cyo	21	
<i>D. melanogaster</i> : 20xUAS-CsChrimson-mVenus	91	
<i>D. melanogaster</i> : pJFRC51-3XUAS-IVS-syt::smHA	74	
<i>D. melanogaster</i> : pJFRC200-10XUAS-IVS-myr::smGFP-HA	74	

REAGENT or RESOURCE	SOURCE	IDENTIFIER
<i>D. melanogaster</i> : pJFRC216-13XLexAop2-IVS-myr::smGFP-V5	74	
<i>D. melanogaster</i> : MCFO-1 [pBPhsFlp2::PEST (attP3);; pJFRC201- 10XUAS-FRT>STOP>FRT-myr::smGFP-HA (VK0005), pJFRC240-10XUAS-FRT> STOP>FRT-myr::smGFP-V5-THS-10XUASFRT>STOP>FRT-myr::smGFP-FLAG (su(Hw)attP1)	74	
Oligonucleotides		
Recombinant DNA		
Software and algorithms		
Matlab 2019a	Mathworks	Mathworks.com
Python		https://www.python.org/
ScanImage 5.1	Vidrio	https://vidriotechnologies.com/scanimage/
Photoshop	Adobe	https://www.adobe.com/products/photoshop.html
ImageJ	NIH	https://imagej.nih.gov/ij/
VVDviewer	Takashi Kawase	https://github.com/takashi310/VVD_Viewer
Computational Morphometry Toolkit	SRI International	https://www.nitrc.org/projects/cmtk/
Other		